

# Advances in Flexible Magnetosensitive Materials and Devices for Wearable Electronics

Huali Yang, Shengbin Li, Yuanzhao Wu,\* Xilai Bao, Ziyin Xiang, Yali Xie, Lili Pan, Jinxia Chen, Yiwei Liu,\* and Run-Wei Li\*

Emerging fields, such as wearable electronics, digital healthcare, the Internet of Things, and humanoid robots, highlight the need for flexible devices capable of recording signals on curved surfaces and soft objects. In particular, flexible magnetosensitive devices garner significant attention owing to their ability to combine the advantages of flexible electronics and magnetoelectronic devices, such as reshaping capability, conformability, contactless sensing, and navigation capability. Several key challenges must be addressed to develop well-functional flexible magnetic devices. These include determining how to make magnetic materials flexible and even elastic, understanding how the physical properties of magnetic films change under external strain and stress, and designing and constructing flexible magnetosensitive devices. In recent years, significant progress is made in addressing these challenges. This study aims to provide a timely and comprehensive overview of the most recent developments in flexible magnetosensitive devices. This includes discussions on the fabrications and mechanical regulations of flexible magnetic materials, the principles and performances of flexible magnetic sensors, and their applications for wearable electronics. In addition, future development trends and challenges in this field are discussed.

foldable characteristics.<sup>[1–3]</sup> This flexibility enables them to conform to various curved surfaces and complex shapes, resulting in a wide range of applications, such as in wearable technology,<sup>[4,5]</sup> healthcare,<sup>[5,6]</sup> smart electronic skin,<sup>[7–9]</sup> the Internet of Things (IoT),<sup>[10,11]</sup> military security,<sup>[12]</sup> and entertainment (human–computer interaction).<sup>[13,14]</sup> Flexible electronics have a wide range of applications in wearable electronics, offering key features and innovations in wearable devices. For example, flexible sensors can monitor physiological data, such as heart rate,<sup>[7,15,16]</sup> body temperature,<sup>[17,18]</sup> blood oxygen saturation,<sup>[6,7,19]</sup> and movement status.<sup>[20–22]</sup> This monitoring is essential for health tracking, disease management, and medical diagnosis. When integrated into textiles to create smart textiles, they can monitor information, such as body temperature, sweat composition, and movement status, transmitting this data to the cloud for analysis.<sup>[23–25]</sup> These innovations have far-reaching implications for

enhancing user experience, quality of life, and driving progress in healthcare.

Further, flexible magnetosensitive devices represent a unique category of electronic devices that combine the properties of flexible electronics and magnetic materials. As electronic skins, magnetic sensing elements are particularly well-suited for contactless human–computer interaction.<sup>[26–28]</sup> These devices typically consist of magnetic elements and flexible substrates, allowing them to exhibit unique properties and application potential in various fields (Figure 1), such as:

- Localization and navigation;<sup>[29,30]</sup> flexible magnetoresistive sensors can be integrated into wearable devices, such as smartwatches and fitness trackers to provide localization and navigation capabilities. They enable compass applications and pedometers by detecting changes in the Earth's magnetic field.
- Health monitoring and biometrics;<sup>[31]</sup> magnetic skin patches can be used to monitor muscle activity and provide valuable data for physiotherapy, sports training, and healthcare. In addition, flexible magnetoelectronic devices can monitor various health parameters, such as heart rate, breathing patterns,

## 1. Introduction

Flexible electronic devices are a cutting-edge class of electronic devices known for their soft, bendable, stretchable, and

H. Yang, S. Li, Y. Wu, X. Bao, Z. Xiang, Y. Xie, L. Pan, J. Chen, Y. Liu, R.-W. Li

CAS Key Laboratory of Magnetic Materials and Devices  
 Ningbo Institute of Materials Technology and Engineering  
 Chinese Academy of Sciences  
 Ningbo 315201, P. R. China

E-mail: [wuyz@nimte.ac.cn](mailto:wuyz@nimte.ac.cn); [liuyw@nimte.ac.cn](mailto:liuyw@nimte.ac.cn); [runweili@nimte.ac.cn](mailto:runweili@nimte.ac.cn)

H. Yang, S. Li, Y. Wu, X. Bao, Z. Xiang, Y. Xie, L. Pan, J. Chen, Y. Liu, R.-W. Li  
 Zhejiang Province Key Laboratory of Magnetic Materials and Application  
 Technology

Ningbo Institute of Materials Technology and Engineering  
 Chinese Academy of Sciences  
 Ningbo 315201, P. R. China

X. Bao, L. Pan, J. Chen, Y. Liu, R.-W. Li  
 College of Materials Sciences and Opto-Electronic Technology  
 University of Chinese Academy of Sciences  
 Beijing 100049, P. R. China

 The ORCID identification number(s) for the author(s) of this article can be found under <https://doi.org/10.1002/adma.202311996>

DOI: 10.1002/adma.202311996

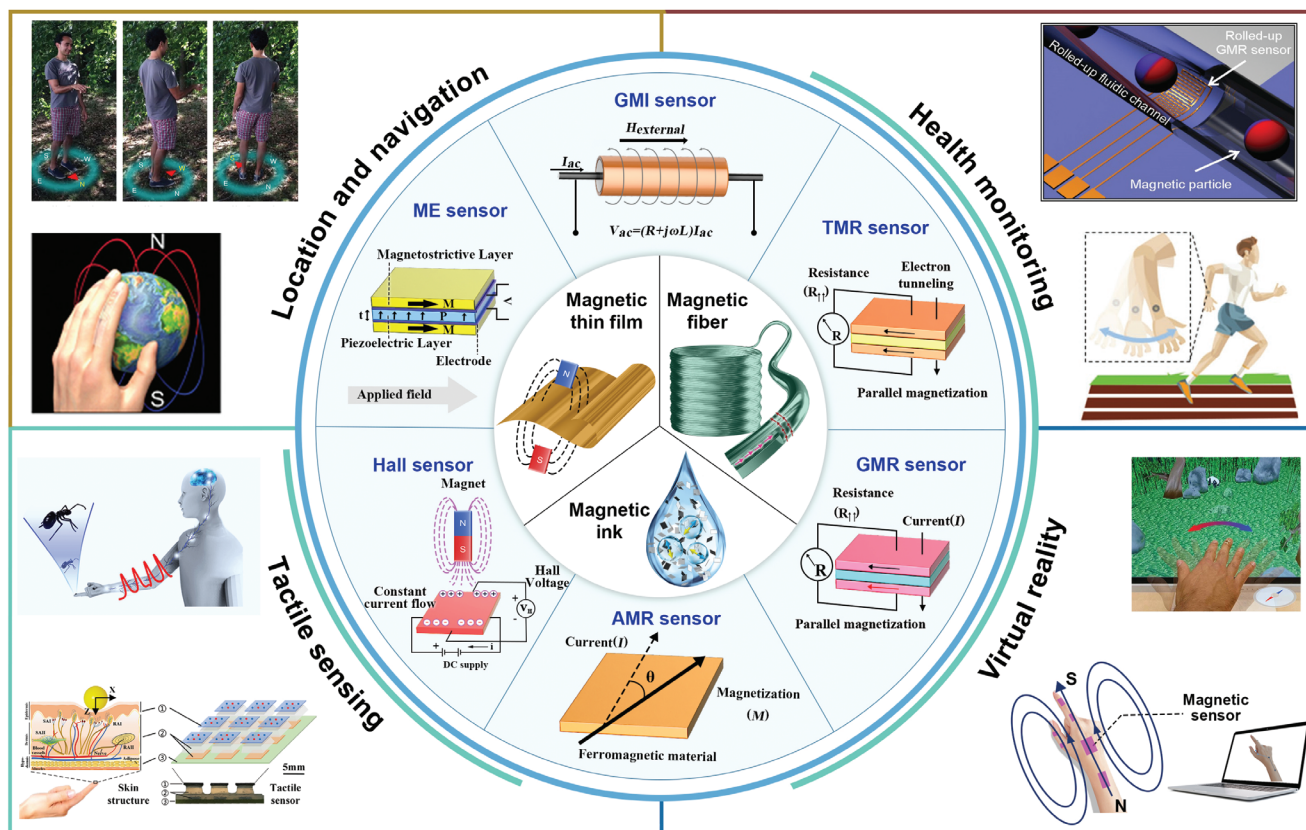


**Figure 1.** Flexible magnetosensitive materials, devices, and applications. By combining the fields of flexible electronics and magneto-electronics, flexible magnetic devices offer a range of advantages, such as re-shapability, conformability, contactless sensing, and navigation capability. These unique properties make these devices ideal for various applications, such as location and navigation.<sup>[27]</sup> Copyright 2021, Wiley-VCH with a Creative Commons CC-BY license. Reproduced with permission.<sup>[29]</sup> Copyright 2018, Springer Nature, healthcare and medical diagnostics. Reproduced with permission.<sup>[186]</sup> Copyright 2020, Wiley-VCH. Reproduced with permission.<sup>[185]</sup> Copyright 2011, American Chemical Society, tactile sensing. Reproduced with permission.<sup>[187]</sup> Copyright 2018, AAAS. Reproduced with permission.<sup>[188]</sup> Copyright 2021, AAAS, AR, and VR. Reproduced with permission.<sup>[29]</sup> Copyright 2018, Springer Nature.

and muscle activity, making them invaluable in medical diagnosis and patient monitoring.

- (c) Gesture control;<sup>[32]</sup> magnetosensitive wearable gloves detect hand movements and gestures. This allows users to control various devices through hand movements, making them ideal for virtual reality (VR) and augmented reality (AR) applications.
- (d) Haptic feedback;<sup>[26,33]</sup> wearable magnetic Haptic feedback devices allow users to feel vibrations, touch, or pressure through a wearable device. This feature is valuable in gaming, immersive experiences, and accessible technologies.

Flexible magnetosensitive materials and devices offer numerous opportunities for enhancing the functionality of wearable electronic devices. These advancements enable new functionalities, enhance the user experience, and contribute to the growing field of wearable technology. Constantly evolving applications make wearable electronics more versatile and capable of satisfying various needs in areas, such as healthcare, entertainment, and sports. This study provides a review of the recent progress in the field of flexible magnetosensitive materials and devices, fo-

cus on the most recent research results over the past 10 years since our previous research.<sup>[34]</sup> Building upon previous studies on flexible magnetosensitive devices,<sup>[27,35–37]</sup> this review provides a thorough overview of the development and research status of flexible magnetosensitive materials, devices, and applications. The remainder of this paper is organized as follows: Section 2 summarizes the fabrication and stress regulation of flexible magnetic materials. Section 3 reviews the principles and key performance characteristics of various flexible magnetic sensors. Section 4 discusses the applications of wearable flexible magnetic sensors. Finally, a summary and future outlook are provided in Section 5.

## 2. Flexible Magnetosensitive Materials

Numerous materials can respond to the application of magnetic fields. For example, magnetoresistive materials demonstrate changes in resistance when subjected to an external magnetic field, whereas magnetostrictive materials exhibit changes in length. In addition, properties such as impedance, optical response, and electric polarization can be influenced by an external magnetic field. Among the numerous magnetosensitive

**Table 1.** Parameters of some magnetic materials and flexible substrates.

Materials	$\alpha$ [ppm K <sup>-1</sup> ]	$E$ [GPa]	$T_g$ [K]	$T_m$ [K]
Fe	11.7	200	–	1813
Co	13.8	211	–	1768
Ni	13.4	210	–	1726
PI	30–60	2.9–20	523	723
PET	20–80	6–14	351	533
PMMA	70–77	2.4–3.4	373	358
PVDF	80–140	2	231	414
PDMS	310	1–3 MPa	123	233
Mica	9	61	–	1503

materials, magnetic materials have garnered significant attention owing to their high magnetic sensitivity. However, most bulk magnetic materials are rigid; to fulfill the increasing demand for flexible and compact magnetic devices in wearable applications, magnetic thin films with considerable mechanical flexibility are attractive.

## 2.1. Preparation of Flexible Magnetic Thin Films

### 2.1.1. Direct Deposition on Flexible Substrates

To retain flexibility, magnetic thin films are typically obtained by sputtering these materials onto flexible substrates, such as polyimide (PI), polyethylene terephthalate (PET), polyvinylidene fluoride (PVDF), and polydimethylsiloxane (PDMS).<sup>[38–41]</sup> During the sputtering process, heat is transferred from the plasma to the substrates, resulting in thermal expansion of the substrates. After growth, the films and substrates cool down to room temperature. Owing to the differences in thermal expansion coefficient ( $\alpha$ ) between the substrates and magnetic films, internal stress appears at their interface. The internal stress may be retained or released depending on the magnitude of the thermal expansion and Young's modulus ( $E$ ) of these materials (Table 1). Based on experimental studies, flat magnetic films can be obtained by direct sputtering onto PET and PI substrates.<sup>[42]</sup> However, for magnetic films deposited directly onto PDMS, irregular wrinkles are formed owing to the significant differences in the thermal expansion coefficient and Young's modulus between PDMS and the magnetic materials. These wrinkles serve to release internal stress (Figure 2a). To achieve a regular pattern, the PDMS substrate can be pre-strained before film deposition. For example, Melzer et al.<sup>[43]</sup> deposited giant magnetoresistance (GMR) multilayer on a PDMS substrate with thermally induced shrinkage, resulting in a wrinkled topography upon peeling off the PDMS substrate from the Si holder (Figure 2b). Zhang et al.<sup>[44]</sup> deposited FeGa films on a uniaxially pre-strained PDMS substrate, producing flexible FeGa films with periodic wrinkles. Li et al.<sup>[45]</sup> demonstrated the excellent stretchability of these devices by preparing spin-valve structures on pre-strained PDMS.

While the aforementioned direct deposition method has been widely adopted by researchers, it has its limitations. First, flexible polymer tapes exhibit higher roughness compared with conventional rigid substrates. Flexible polymeric substrates, such as

PET and PI, exhibit typical root-mean-square roughness of 1–2 nm,<sup>[39,46]</sup> much larger than the  $\approx 0.3$  nm roughness of thermally oxidized Si substrates. This increased roughness is particularly crucial when growing multilayered heterostructures as the properties significantly depend on the interface quality. Therefore, special treatments are necessary to fabricate high-quality multilayered heterostructures. Second, interfacial intermixing is a concern. The loose atomic structures of flexible substrates enable magnetic atoms to easily penetrate the polymer substrate, leading to intermixing. Consequently, growing ultra-thin magnetic films down to a few atomic layers is not suitable in this scenario. Third, the inability to withstand high temperatures is a common issue with flexible substrates, such as PET, PVDF, PI, and PDMS (Table 1). However, in the fabrication of high-performance spintronic devices, post-thermal annealing is often required. In addition, a high growth temperature is critical for preparing magnetic films with superior crystal quality (such as single-crystalline films), which are essential for achieving outstanding performance in spintronic devices, such as antiferromagnetic magnetic tunneling junctions. These requirements are difficult to achieve through deposition on flexible polymers.

### 2.1.2. Deposit and Transfer to Flexible Substrates

To address the limitations of direct deposition methods, the transfer method is developed. In the transfer method, magnetic films are initially deposited on rigid substrates capable of withstanding high temperatures. Subsequently, the films are detached from the substrates and transferred onto the surfaces of flexible substrates. To facilitate this transfer process, magnetic films should be deposited on substrates with weak interactions with the film and substrates buffered with a sacrificial layer.

Experimental findings revealed that epitaxial growth is achievable for some 2D substrates with van der Waals interlayer interactions, despite the different lattice constants and symmetries of the films. In addition, the weak van der Waals forces bonding the films and 2D substrates enable the transfer of films onto various support substrates. For example, mica, a commercially available 2D material with an exceptionally high melting point (Figure 2c and Table 1) serves as an ideal host substrate for the fabrication of various magnetic films and devices.<sup>[47,48]</sup> Further, the weak interaction between mica and film allows for the elimination of lattice mismatch and substrate clamping effects, resulting in the production of high-quality free-standing films. To date, high-quality oxide magnetic films, such as Fe<sub>3</sub>O<sub>4</sub>,<sup>[49]</sup> CoFe<sub>2</sub>O<sub>4</sub>,<sup>[50]</sup> SrRuO<sub>3</sub>,<sup>[51]</sup> Pr<sub>0.5</sub>Ca<sub>0.5</sub>MnO<sub>3</sub>,<sup>[52]</sup> and VO<sub>2</sub><sup>[53]</sup> have been successfully prepared using mica as the substrate (Figure 2d). These films are ideal for use in flexible magnetoelectronic devices. In addition to oxides, mica substrates have been employed to fabricate flexible magnetic alloys that require high-temperature growth. For example, to retain the desired antiferromagnetic (AFM)-ferromagnetic (FM) phase transition near room temperature, FeRh films must be grown at high temperatures to maintain atomic order.<sup>[54]</sup> Recently, Huang et al.<sup>[55]</sup> fabricated FeRh films with high crystal quality on mica substrates and successfully transferred them onto PDMS substrates by peeling off the Mica with PI tape. In addition to mica, graphene serves as another commonly used van der Waals heteroepitaxial substrate.

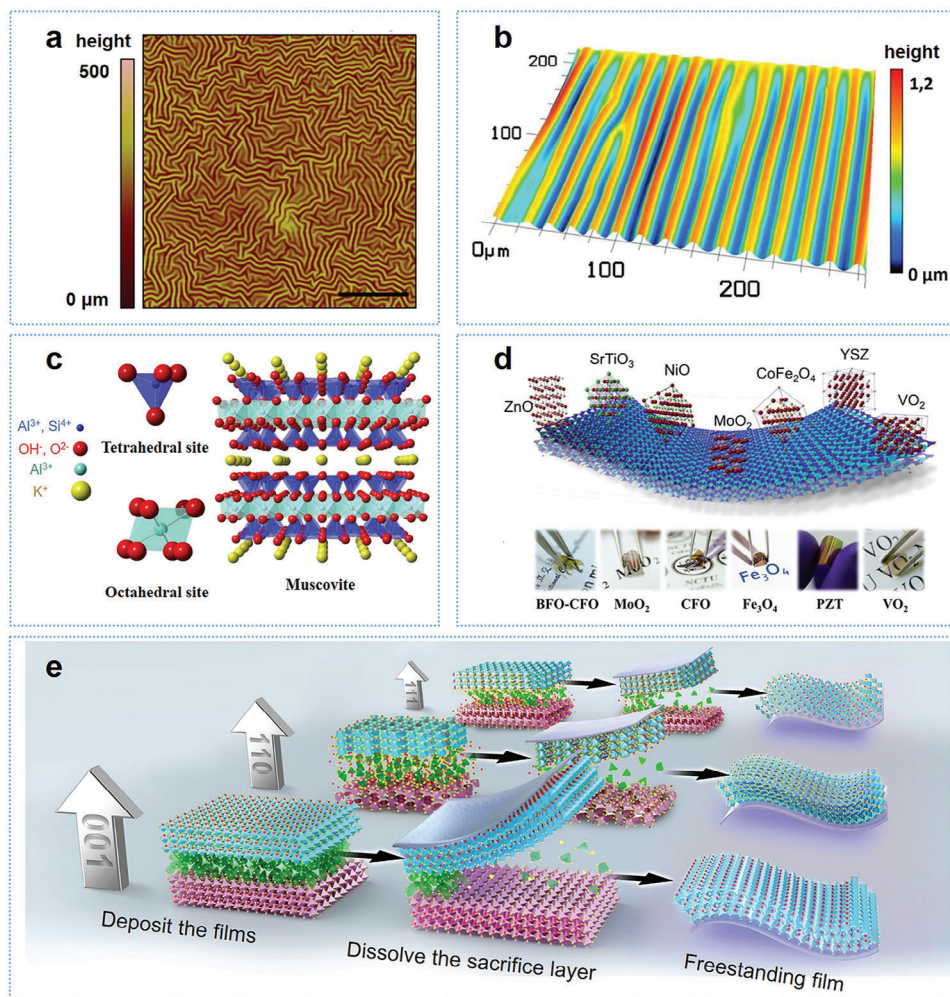


**Figure 2.** a) Topography of magnetic films deposited directly on elastic substrates, such as PDMS.<sup>[41]</sup> Copyright 2012, Wiley-VCH with a Creative Commons CC-BY license. b) Surface image of magnetic films deposited on pre-strained PDMS. Reproduced with permission.<sup>[43]</sup> Copyright 2011, American Chemical Society. c) Layered crystal structure of mica. d) Summary of typical flexible oxide films grown on mica substrates.<sup>[48]</sup> Copyright 2017, Springer Nature with a Creative Commons CC-BY license. e) Fabrication process of the freestanding single crystalline films by dissolving the sacrificial layer.<sup>[65]</sup> Copyright 2022, Springer Nature with a Creative Commons CC-BY license.

In 2020, Kum et al.<sup>[56]</sup> prepared a heterogeneous structure composed of functional layer/graphene/STO. With the presence of the graphene interlayer, freestanding membranes with high crystal quality, including SrTiO<sub>3</sub>, BaTiO<sub>3</sub>, CoFe<sub>2</sub>O<sub>4</sub>, and YIG, could be obtained using mechanical lift-off techniques. In 2021, Du et al.<sup>[57]</sup> successfully prepared a free-stranding Heusler alloy, GdPtSb, using this method and introduced strain gradients into GdPtSb to induce ferromagnetism. This method enables the production of high-quality flexible films with controllable structures and orientations, making it a promising technique for the preparation of industrial materials and the development of novel functional devices. This method is exclusively performed in deionized water, which is more suitable for practical applications owing to its low cost and minimal chemical damage to the oxide film. In addition to the aforementioned 2D substrates, the concept of low adhesion of metal layers (e.g., Cu, Ni, and Au) on SiO<sub>2</sub> has been proposed as an efficient method for transferring thin films and heterostructures onto flexible substrates through mechani-

cal peel-off.<sup>[58–60]</sup> For example, the utilization of a low-adhesion Au underlayer has been proven effective in fabricating spin-valve stacks on large-area flexible substrates.<sup>[58,61]</sup>

Materials, such as MgO,<sup>[62]</sup> La<sub>0.67</sub>Sr<sub>0.33</sub>MnO<sub>3</sub>,<sup>[63]</sup> and Sr<sub>3</sub>Al<sub>2</sub>O<sub>6</sub><sup>[64,65]</sup> can be dissolved in acid, alkaline solvents, or water, serving as sacrificial layers to facilitate the transfer of films onto flexible substrates. While lattice mismatch must be carefully considered for growing high-quality sacrificial layer and magnetic films, the preparation of flexible oxide films featuring different crystallographic directions and structural systems has been achieved. Examples include La<sub>0.67</sub>Sr<sub>0.33</sub>MnO<sub>3</sub><sup>[66]</sup> and SrRuO<sub>3</sub><sup>[65]</sup> films with various crystallographic directions, Sr<sub>2</sub>IrO<sub>4</sub> film with a Ruddlesden–Popper structure,<sup>[67]</sup> super-elastic Fe<sub>3</sub>O<sub>4</sub> with a spinel structure,<sup>[68]</sup> and super-stretchable La<sub>0.7</sub>Ca<sub>0.3</sub>MnO<sub>3</sub> film with a chalcopyrite structure,<sup>[69]</sup> showcasing excellent versatility. For example, Lu et al.<sup>[65,66]</sup> deposited single-crystal La<sub>0.7</sub>Sr<sub>0.3</sub>MnO<sub>3</sub> and SrRuO<sub>3</sub> films onto Sr<sub>3</sub>Al<sub>2</sub>O<sub>6</sub> buffered SrTiO<sub>3</sub> substrates with different crystallographic orientations

([001], [110], and [111]). Following the growth, the bilayers were immersed in pure water to etch the sacrificial  $\text{Sr}_3\text{Al}_2\text{O}_6$  layers. During the etching process, flexible PDMS was utilized as a support layer to mechanically stabilize the films (Figure 2e). The flexible SrRuO<sub>3</sub> membranes exhibited highly adjustable magnetic anisotropy (MA) owing to the cooperative effect of crystal structure and orientation. This resulted in a remarkable perpendicular magnetic energy of  $\approx 10^7$  erg·cm<sup>-3</sup>, allowing for a wide range of tunability from in-plane to out-of-plane orientations.

To prepare sensitive tunneling magnetoresistance (TMR) devices, a high-quality barrier layer, such as  $\text{AlO}_x$  and MgO must be grown at high growth temperatures, presenting a challenge in the preparation of flexible TMR devices. Loong et al.<sup>[70]</sup> successfully transferred magnetic tunnel junction (MTJ) stacks onto a series of plastic substrates by removing the Si substrate through dry etching, followed by the transfer of the suspended stacks onto plastic substrates. The reported TMR was 300% after being transferred onto PET substrates, a significant improvement compared with TMR directly deposited onto PI substrates.<sup>[71]</sup> In addition to the aforementioned sacrificial layers, flexible magnetic films could be obtained by growing them on water-soluble salt substrates, such as NaCl<sup>[72]</sup> and KBr.<sup>[61]</sup>

Despite the significant progress made through transfer approaches, some limitations are worth addressing.<sup>[61]</sup> First, the multi-step fabrication processes involved are unsuitable for mass production. Second, this process often results in reduced surface area coverage. For example, freshly cleaved mica foils consist of extended, micrometer-sized atomic flat terraces that are difficult to control, leading to inconsistent electrical behavior. For the water-soluble KBr substrate, the cleavage steps induce inhomogeneity and layer intermixing in the deposited thin film, which can lead to open-circuit electric behavior at micrometric distances.

### 2.1.3. 3D Self-Assembled Magnetic Field Sensors

New materials and technologies are required to enhance the performance of integrated devices and achieve smaller and lighter designs. These materials and technologies should offer more 3D structural freedom compared with conventional microelectronics as well as simpler parallel manufacturing routes; while, maintaining compatibility with existing methods. Various 3D self-assembly methods for transforming planar membranes into complex 3D structures have been investigated<sup>[73]</sup> (Figure 3a,b). One such method is the rolling-up technology, which utilizes thin-film deposition techniques, such as sputtering, to create magnetic tubes with high structural quality and low surface roughness. Based on previous studies, the magnetic domain patterns of tubular structures are not influenced by the structural inhomogeneities due to the granular nature of the magnetic films. By using different materials and tuning the dimensions of the rolled-up nanomembranes, domain patterns consisting of spiral-like and azimuthally magnetized domains are observed. In particular, azimuthally magnetized rolled nanofilms are highly promising for magnetoimpedance-based field sensors owing to their enhanced isotropic sensitivity compared with planar structures (Figure 3c)<sup>[74]</sup>.

### 2.1.4. Printed Flexible Magnetic Field Sensors

Printed electronic devices have enabled the fabrication of large-scale, low-cost electronic devices on various substrates, playing a crucial role in the advancement of flexible electronics and stretchable electronics.<sup>[75]</sup> Printable magnetic sensing devices are the building blocks for realizing entirely printable electronics.

Karnaushenko et al.<sup>[76]</sup> developed a multicomponent magnetic ink containing GMR flakes and fabricated the first printable magnetic sensor. The fabricated sensor had a room-temperature GMR of up to 8% and adhered to arbitrarily shaped surfaces for contactless switching in electronic circuits. The essential magnetic ink necessary for the development of printable magnetic sensors was prepared by blending the GMR powder with a binder solution. This solution was composed of an acrylic rubber based on poly(methyl methacrylate) (PMMA) dissolved in a methyl isobutyl ketone carrier.<sup>[76,77]</sup> Further, by optimizing the polymeric binder solution and components of the magnetosensitive powder (Figure 4a), high-performance printable GMR sensorics with a GMR ratio of  $\approx 37\%$  at  $-600$  mT were fabricated. The maximum sensitivity of the sensors was  $0.93$  T<sup>-1</sup> at 130 mT, comparable to state-of-the-art high-performance GMR sensors.<sup>[78]</sup> Ha et al.<sup>[79]</sup> prepared magnetic paste by blending GMR microflakes with a binding elastomer of poly(styrene-butadiene-styrene) (SBS) and printed GMR sensors on ultrathin 3  $\mu\text{m}$  thick polymeric foils. The unique mechanical compliance of these printed GMR sensors allowed them to withstand extreme mechanical deformation of up to 16  $\mu\text{m}$  of bending radii. This makes them ideal for use in wearable interactive electronics as they can follow the radial buckling pattern on the stretchable substrates, enabling a stable magnetic field sensing capability under 100% of the biaxial strain (Figure 4b). The application of printed magnetoelectronics has been hindered by the lack of large-area exchange-coupled metallic multilayers required to produce printable magnetosensory inks. To address this challenge, Gupta et al.<sup>[80]</sup> developed a large-scale roll-to-roll process for fabricating large-area GMR thin-film stacks (Figure 4c). The roll-to-roll sputtered multilayer on a hundred-meter-long PET web showed a GMR ratio of  $\approx 40\%$  and was successfully converted to magnetosensitive ink for printing high-performance magnetic sensors, facilitating integration with printed electronics.

The development of printable and compliant high-performance magnetic field sensors utilizing various magnetoresistive effects, in addition to GMR sensors, holds significant potential for expanding their applications. For example, Oliveros Mata et al.<sup>[81]</sup> introduced a novel magnetoresistive paste based on the anisotropic magnetoresistance (AMR) effect by incorporating Py powders into the SBS elastomer matrix. Sensors printed with this paste demonstrated a stable AMR value of 0.34% at 400 mT even under mechanical bending, making them ideal for use on curved surfaces for on-skin applications and interactive printed electronics (Figure 5a). Further, Xu et al.<sup>[82]</sup> extended the performance of printable AMR sensors by adopting alternating magnetic fields (AMFs) to actively manipulate the magnetoresistive fillers (Figure 5b). The resulting sensors exhibited superior magnetoresistive performance, with a sensitivity of  $35.7$  T<sup>-1</sup> at 0.086 mT, low noise of 19  $\mu\Omega$  per  $\sqrt{\text{Hz}}$ , and high resolution of 36 nT. The utilization of AMF also facilitated the self-healing capability of the magnetic paste, enabled by

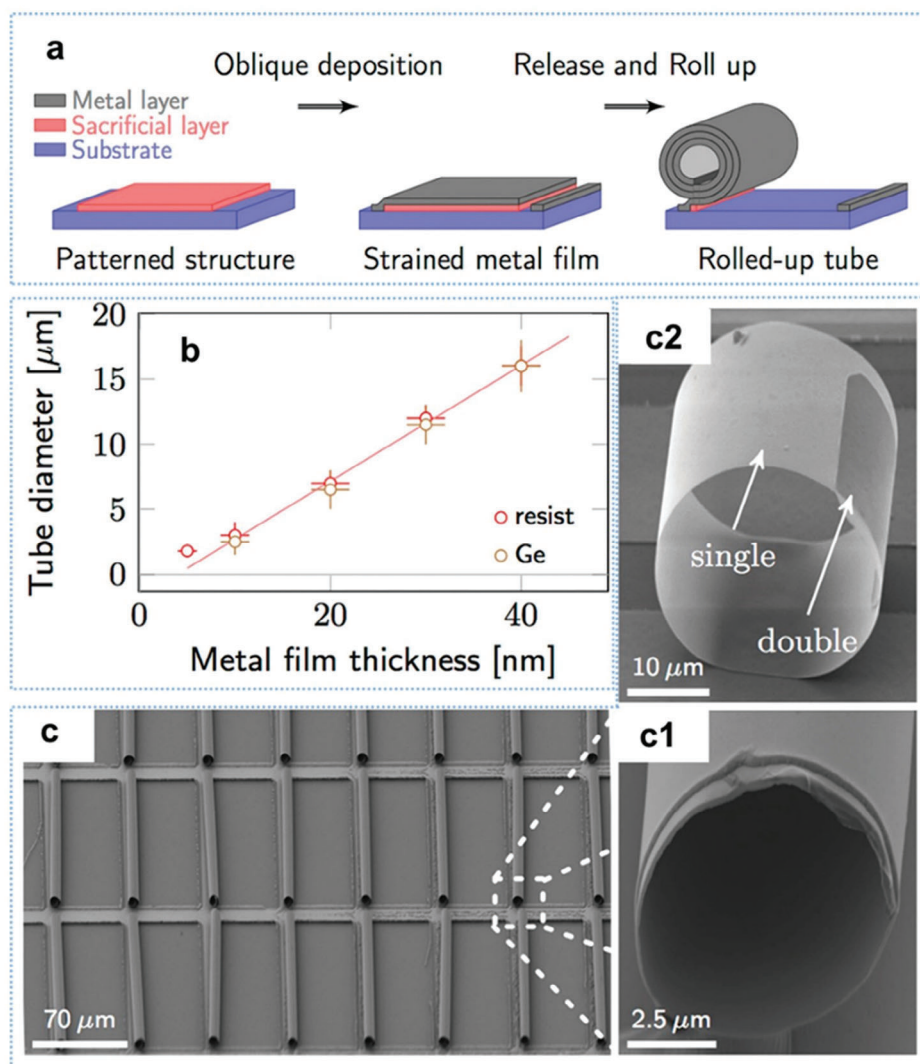


**Figure 3.** Fabrication of rolled-up single-layer ferromagnetic nanomembranes. a) Schematic of the fabrication process. b) Dependence of the rolled-up nanomembrane diameter on film thickness. c) SEM images of the rolled-up tubes.<sup>[74]</sup> Copyright 2014, Wiley-VCH with a Creative Commons CC-BY license.

the viscoelastic supramolecular polyborosiloxane. Six characteristics were revealed in AMF-mediated self-healing: 100% performance recovery, repeatable healing over multiple cycles, room-temperature operation, healing in seconds, no manual reassembly required, and humidity insensitivity. These characteristics paved the way for printable magnetoresistive sensors in various applications, such as bio-monitoring, smart textiles for safety applications, medical therapy, and human-machine interfaces for AR. Mata et al.<sup>[83]</sup> reported dispenser printing of a bismuth-based paste at a commodity scale, processed through laser sintering to obtain printed magnetoresistive sensors. In contrast to previously printed magnetic sensors, bismuth sensors exhibited up to a 146% resistance change at 5 T at room temperature. This resulted from the unique large quantum orbital magnetoresistive effect, enabling their operation in high magnetic fields, such as during magnetic resonance imaging and nuclear magnetic resonance.

Various flexible magnetic films and devices prepared using the aforementioned methods, along with their bending or stretching capabilities are listed in **Table 2**. Advances in film preparation technology have increased the tensile limit of flexible metallic magnetic films and enhanced their multidirectional stretching capabilities. These properties provide a better material basis for the application of flexible magnetic films in stretchable electronic devices.

## 2.2. Effect of Stress/Strain on the Magnetic Properties of Flexible Magnetic Films

Unlike rigid substrates, flexible magnetic films are subjected to mechanical stress upon deformation, which influences their magnetic properties. In particular, some magnetic properties, such as the magnetic transition temperature, confine the

**Table 2.** Preparation of flexible magnetic films and devices along with their stretching capabilities.

Material and preparation method		Strain limitation		Ref.
		Single axis	Dual axis	
Metal and alloy	CoFeB directly deposited on PI	1.6%	–	[5]
	Co directly deposited on PET	2%	2%	[7]
	Spin valve with periodic cracks	29%	–	[1]
	Spin valve with periodic wrinkles	50%	–	[2]
	GMR transferred onto VHB	270%	–	[10]
Oxides	BaM grown on mica	1.3%	–	[96]
	La <sub>0.7</sub> Ca <sub>0.3</sub> MnO <sub>3</sub> transferred onto polyimide	8%	5%	[194]
	BiMnO <sub>3</sub> transferred onto PDMS	5.1%	–	[195]

working temperature; magnetic anisotropy (MA) influences the sensitivity, operating frequency, and even power consumption, whereas the Dzyaloshinskii–Moriya interaction (DMI) determines the chirality and topological features of the magnetic structure. The aforementioned properties determine the performance of magnetic devices. In addition, the spin–orbit coupling strength and electronic structure of nonmagnetic materials are extremely crucial in constructing spin-orbit torque devices. Therefore, understanding the mechanical regulation of these properties in flexible magnetic films is essential.

### 2.2.1. Stress/Strain Modulation of the MA in Flexible FM Films

In 2012, Dai et al. deposited FeGa films on flexible PET substrates and investigated the effect of mechanical bending on the MA.<sup>[39]</sup> As shown in the inset of **Figure 6a**, various strains were exerted on the FeGa films by bending the PET on molds with different radii of curvature. They observed that the unstrained Fe<sub>81</sub>Ga<sub>19</sub> films displayed unique uniaxial MA attributed to the residual stress in the PET substrates. By applying tensile (compressive) strains along the easy axis, the magnetic easy (hard) axis could be adjusted to the hard (easy) axis. By calculating the MA constant of flexible FeGa films under various stress conditions, Cao et al. estimated the magnetostriction coefficient to be ≈80 ppm.<sup>[84]</sup> For flexible single-layer magnetic films, the mechanical regulation of MA correlated with the magnetostriction coefficients. For example, flexible magnetic films with positive magnetostriction coefficients, such as CoFeB,<sup>[85]</sup> Fe,<sup>[86]</sup> and Co<sup>[87]</sup> exhibited similar mechanical stress regulation on their MA to FeGa. Conversely, flexible magnetic films with negative magnetostric-

tion coefficients, such as Ni,<sup>[88,89]</sup> showed a tendency for the easy axis to rotate perpendicular to applied tensile stress. In particular, the MA of NiFe films with a nearly zero magnetostriction coefficient remained unaffected by external stress.<sup>[90]</sup> Compared to that of flexible magnetic metals and alloys, the stress regulation of the MA of flexible magnetic oxides was more versatile owing to the intimate coupling among the lattice, spin, orbit, and charge.<sup>[91,92]</sup>

In addition to the aforementioned flexible magnetic films that exhibit dominant in-plane MA, flexible magnetic films with perpendicular magnetic anisotropy (PMA) are gaining attention for their potential in developing spintronic devices with high density and stability. Several studies on stress regulation by PMA in flexible magnetic films have been conducted. For example, Ota et al.<sup>[93]</sup> conducted experiments in which TbFeCo (6 nm) and Pt/Co (0.4–0.9 nm)/Pt films with PMA were deposited on flexible polyethylene naphthalate (PEN) substrates. They observed a significant change in the magnetic easy axis orientation from out-of-plane to in-plane in TbFeCo when a 2% in-plane uniaxial strain was applied, whereas the PMA of the Pt/Co/Pt films was maintained. Matsumoto et al.<sup>[94]</sup> observed that for Pd/Co (1.5 nm)/Pd deposited on flexible PEN substrates, the pristine in-plane MA was tuned to PMA under the application of 1.5% biaxial tensile strain and that biaxial strain was more effective than uniaxial strain in tuning the MA of flexible magnetic films.<sup>[94]</sup> More recently, Li et al.<sup>[40]</sup> conducted a systematic study of the stress regulation of MA in Co/Pt multilayers. By depositing Ta (2 nm)/Pt (20 nm)/[Co (*t*)/Pt (0.5 nm)]<sub>4</sub>/Pt (1.5 nm) multilayers on flexible PVDF substrates, they achieved modulation of the MA from in-plane to out-of-plane by varying the Co thickness (*t*) from 0.6 to 3.0 nm. From both magnetic hysteresis and magnetic domain measurements, they observed that while a robust PMA was maintained against external stress, the MA became more susceptible to external stress as the Co thickness increased.

The effect of mechanical stress on the modulation of the MA can be quantitatively assessed by calculating the slope of the MA constant ( $K_u$ ) with respect to stress. The  $K_u$  value of flexible magnetic films can be estimated using either magnetic hysteresis measurements along different directions<sup>[39]</sup> or anisotropic magnetoresistance measurements.<sup>[87]</sup> In the former method, the strength of a uniaxial anisotropy can be quantitatively evaluated by calculating the difference between works done in magnetization along the easy axis and hard axis:  $K_u = \mu_0 \left( \int_0^{M_s} H_{//e.a.} dM - \int_0^{M_s} H_{//h.a.} dM \right)$ , where  $\mu_0$  represents the permeability of free space,  $M_s$  represents the saturation magnetization moment, and  $M$  denotes the virgin magnetization moment that can be obtained approximately by averaging the upper and lower branches of the hysteresis loops. In the latter method, the strength of MA is correlated to the magnetic torque of the film as follows:  $L(\theta_M) = \mu_0 M_s H \sin(\theta_H - \theta_M) = K_u \sin(2\theta_M)$ , where the relationship between the applied magnetic field direction ( $\theta_H$ ) and film magnetic moment direction ( $\theta_M$ ) can be established through AMR measurements.

A summary of the strain-dependent anisotropy constant  $K_u$  for certain flexible magnetic films is shown in **Figure 6b**.<sup>[39,87,89,93–96]</sup> First, strain-induced MA is significant for most reported flexible magnetic films. Second, for different materials, the slope of the MA constant with respect to stress (that is, the stress

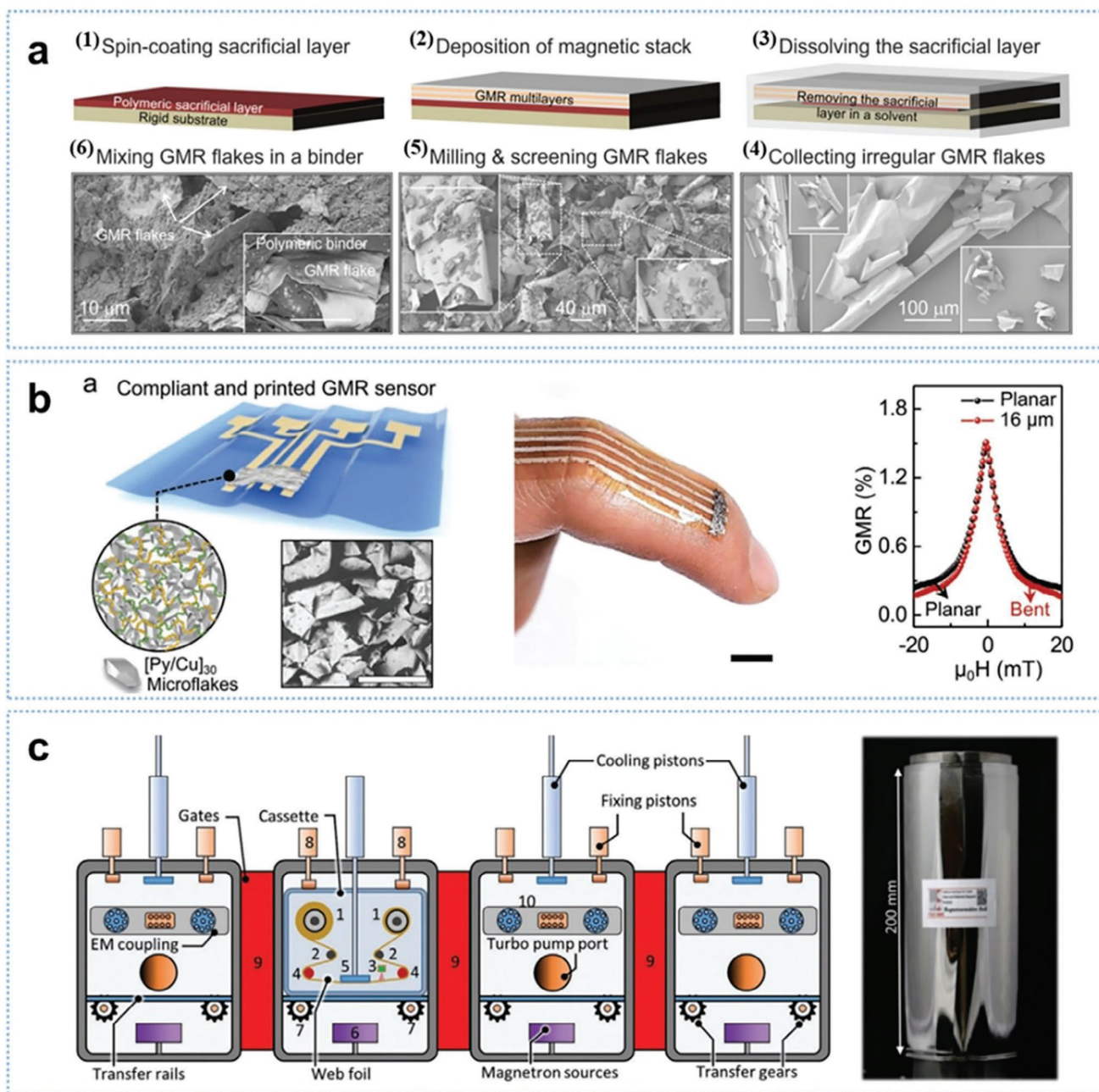


**Figure 4.** a) Printable GMR sensors and devices. Schematics of the fabrication process of the GMR paste.<sup>[78]</sup> Copyright 2015, Wiley-VCH with a Creative Commons CC-BY license. b) Printed GMR sensors that conform to the finger and their performance.<sup>[79]</sup> Copyright 2021, Wiley-VCH with a Creative Commons CC-BY license. c) Schematics of the cassette-based roll-to-roll modular sputter system and of the deposited GMR multilayer on a  $0.2 \times 100 \text{ m}^2$  PET web.<sup>[80]</sup> Copyright 2022, Wiley-VCH with a Creative Commons CC-BY license.

coefficient of magnetoelastic anisotropy) differs. Third, the strain stability of the MA can be significantly enhanced by the structural design. For example, the variation in the MA of a CoFeB film is as high as  $2 \times 10^5 \text{ erg cm}^{-3}$  under 0.5% strain, and the film can only withstand less than 2% strain.<sup>[87]</sup> However, if CoFeB films are designed with a wrinkled structure, they can withstand more than 50% strain, and the change in MA is less than  $10^4 \text{ erg cm}^{-3}$ .<sup>[95]</sup> Therefore, the structural design is crucial in improving film stretchability. The stress coefficients of typical ferromagnetic

thin films (Fe, Co, Ni, and CoFeB) are shown in Figure 6c. Among the materials investigated, Fe has the lowest stress coefficient of  $\approx 6.3 \times 10^3 \text{ erg cm}^{-3} \text{ GPa}^{-1}$ , whereas Ni has the highest stress coefficient of up to  $2.5 \times 10^5 \text{ erg cm}^{-3} \text{ GPa}^{-1}$ .

Changes in MA are also accompanied by variations in magnetic resonance behavior.<sup>[95,97–99]</sup> This finding provides a basis for developing flexible devices with tunable resonance frequencies; thus, opening up potential applications in microwave generators, microwave detectors, resonators, and other related devices.

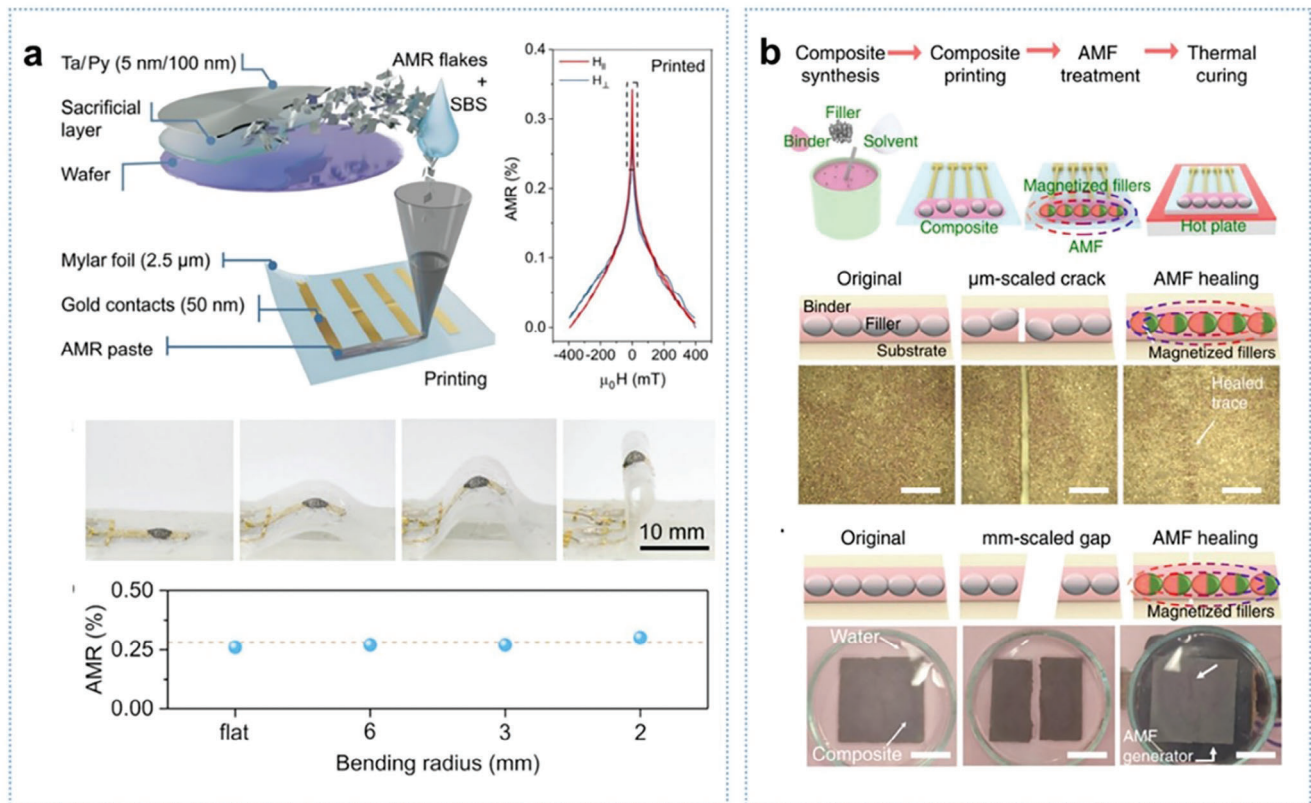


**Figure 5.** Printable and self-healable AMR sensors. a) Fabrication process of the printed AMR sensor as well as its response to an in-plane magnetic field and the bending state.<sup>[81]</sup> Copyright 2021, Springer Nature with a Creative Commons CC-BY license. b) Fabrication and self-healing of magneto-resistive sensors aided by alternating magnetic fields.<sup>[82]</sup> Copyright 2022, Springer Nature with a Creative Commons CC-BY license.

### 2.2.2. Stress/Strain Modulation of the MA in Flexible AFM Films

Compared with ferromagnetism, antiferromagnetism offers advantages, such as magnetic field insensitivity, zero stray fields, and ultrafast dynamics and is considered a vital material for realizing high-density storage and terahertz devices. However, effectively manipulating and observing AFM moments is challenging owing to the zero net magnetic moment of antiferromagnetism and its insensitivity to external magnetic fields. The exchange

bias effect is generated between the AFM and FM interfaces, resulting in unidirectional MA of FM films, which is widely utilized in giant magneto-resistive devices.<sup>[100,101]</sup> Further, the exchange spring structure in antiferromagnetism will be formed owing to the exchange bias effect, which facilitates the observation and manipulation of AFM moments.<sup>[102]</sup>

Zhang et al.<sup>[103]</sup> observed an increasing remanence ratio and a decreasing exchange bias field along the pinning direction when the compressive strain was applied perpendicular to the

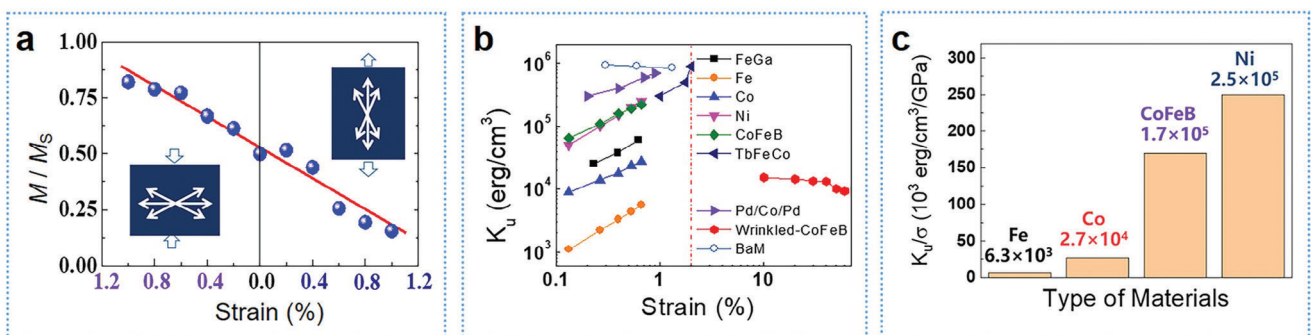


**Figure 6.** Effect of mechanical strain on the MA of flexible magnetic films. a) Evolution of the remnant magnetization ratio under different strains. The insets represent the schematic model showcasing the distribution of magnetization moments at different strains. b) Regulation of the MA by external strain in different flexible magnetic films. The vertical dashed line represents the maximum tensile strain without a crack in bulk metals. Reproduced with permission.<sup>[189]</sup> Copyright 2021, Acta Physica Sinica. c) Comparison of the stress coefficient of different materials.

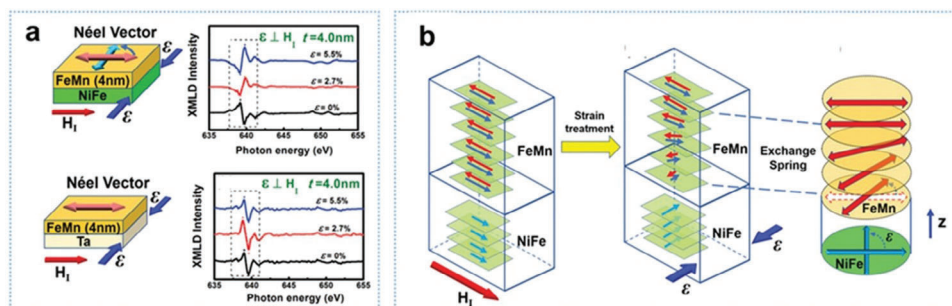


**Figure 7.** a) Strain-related antiferromagnetic moment tunability. Schematic of the Néel vector in FeMn and corresponding Mn L-edge XMLD spectra with the application of strain. b) Schematic model of the strain control of the antiferromagnetic moment and exchange spring in FeMn. Reproduced with permission.<sup>[106]</sup> Copyright 2020, Wiley-VCH.

pinning direction. The simulation results based on the Stoner–Wohlfarth model indicate that the different responses of FM and AFM moments to external strain weakened the pinning effect, thereby reducing the exchange bias field. Sheng et al.<sup>[104]</sup> deposited exchange biased CoFeB/IrMn heterostructures on PVDF substrates and measured the magnetic hysteresis loop of the pinned CoFeB layer to determine the magnetic moment arrangement of the IrMn layer. Owing to the anisotropic thermal expansion of the PVDF substrate, uniaxial compressive stress was exerted by varying the temperature of the sample. Through magnetic field orientation dependence of hysteresis loop measurements, a rotation of  $10^\circ$  was observed in IrMn moments under 2.26 GPa compressive stress. In a related study, Zhang et al.<sup>[105]</sup> observed a  $12^\circ$  rotation in the IrMn moments under  $\approx 0.6\%$  compressive strain through ferromagnetic resonance measurements. In a study by Feng et al.,<sup>[106]</sup> the X-ray linear magnetic dichroism (XMLD) technique was utilized to evaluate the effective tunability of the AFM moment of FeMn by controlling the exchange spring in NiFe/FeMn with a large strain exerted by a shape-memory alloy substrate (Figure 7a). The strain toggled a noticeable magnetic moment rotation of NiFe by nearly  $90^\circ$  in the film plane, resulting in a consequent twirling of the Néel vector of FeMn owing to the interfacial exchange interaction (Figure 7b).

### 2.2.3. Stress/Strain Modulation of the DMI

The DMI prefers the canting of the spins of adjacent magnetic atoms and is recognized as a key ingredient in forming localized noncollinear magnetic structures, such as chiral domain walls and magnetic skyrmions, which holds significant promise for various applications, such as memory and logic. Physically, DMI originates from spin–orbit coupling and relies on broken inversion symmetry. Based on previous studies, the application of strain can influence the DMI both in bulk crystals and heavy metal–FM multilayer structures.

Gusev et al.<sup>[107]</sup> performed Brillouin light scattering and magneto–optical Kerr effect studies on mechanically bent Pt/Co/Pt films and observed that the uniaxial strain modified the average DMI constant and introduced anisotropy to the DMI (Figure 8a). They interpreted the microscopic nature of the strain-modulated DMI using the Fert–Levy model. Based on this model,

the DMI is mediated by the hopping of electrons between magnetic ions and heavy-metal ions, which relies on the distances between the magnetic ions and those between the magnetic and heavy-metal ions. These distances can be changed by applying an in-plane strain, thereby modifying the DMI, as shown in Figure 8b. Sapozhnikov et al.<sup>[108]</sup> further investigated the influence of strain-induced anisotropic interfacial DMI on the magnetic domain structures in Co/Pt multilayers by utilizing magnetic force microscopy (MFM) and observed the transformation of an isotropic labyrinth domain structure to oriented stripe domains and zigzag domain structures under strain application.

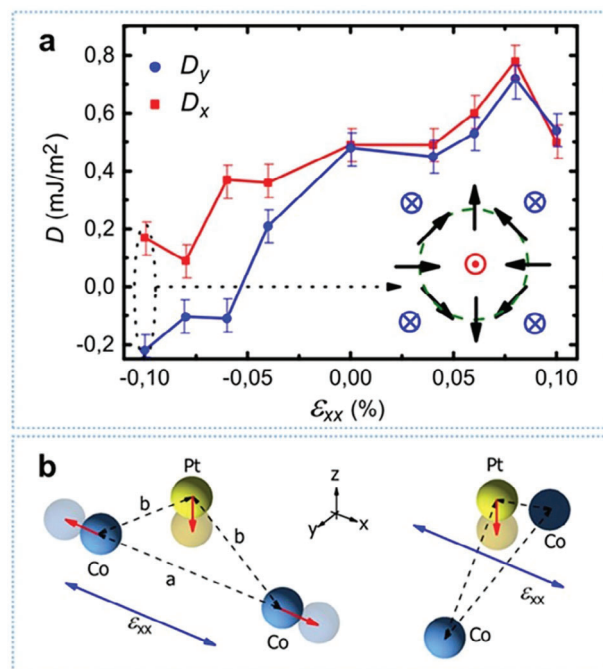


**Figure 8.** a) DMI constant measured along the  $x$ - and  $y$ -axes as a function of applied strain ( $\epsilon_{xx}$ ). Notably, the DMI constant exhibits an anisotropic response to compressive strain. b) Displacement of Co and Pt ions owing to the tensile strain  $\epsilon_{xx}$ , with the ion triangle oriented along (left) and perpendicular (right) to the  $x$ -axis.  $a$  and  $b$  denote the distance between Co ions and that between Pt and Co ions, respectively. Reproduced with permission.<sup>[107]</sup> Copyright 2020, American Physical Society.

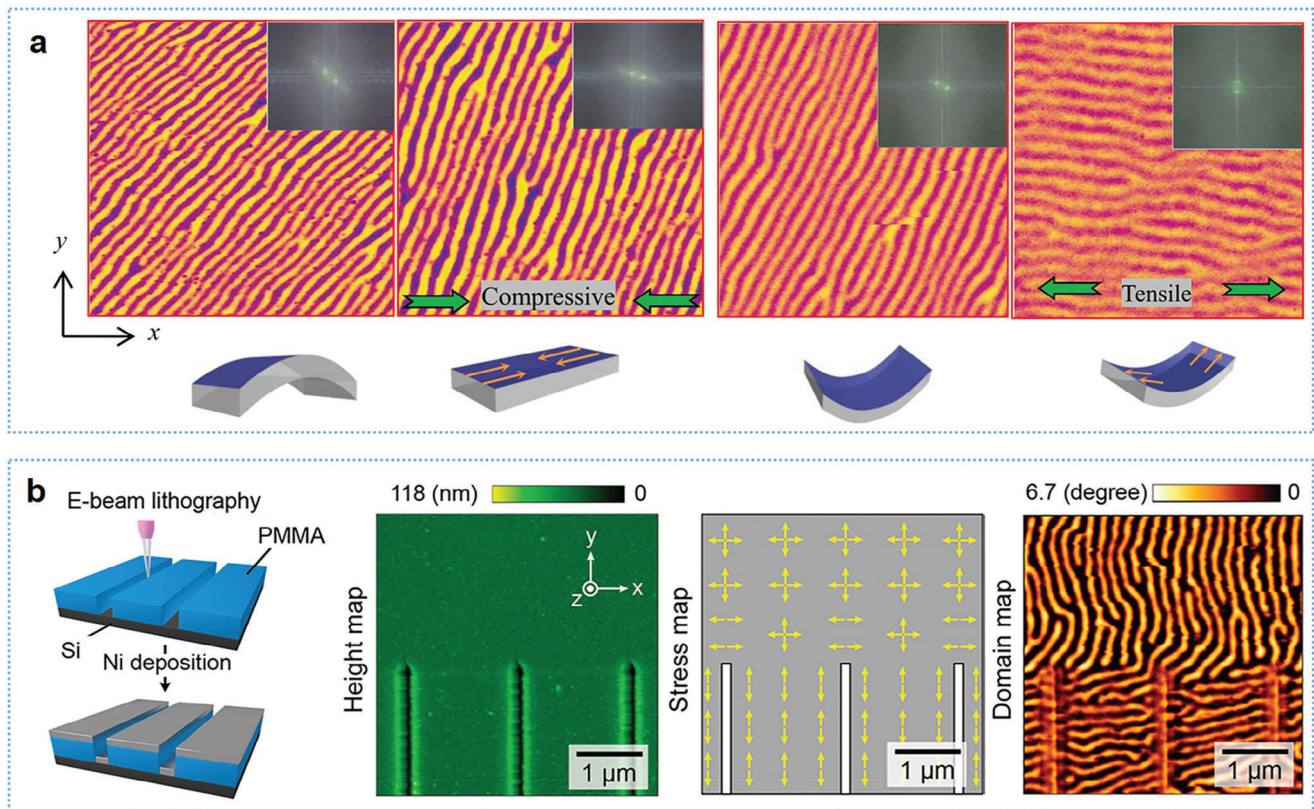


**Figure 9.** a) Magnetic domain structure of the FeGa film with different stress states (from left to right): attached on a convex mold and flattened, removed from the convex mold and flattened, attached on a concave mold, and removed from the concave mold and flattened. Reproduced with permission.<sup>[190]</sup> Copyright 2019, IOP Publishing. b) Modulation of the magnetic domain structure of Ni films with micro-patterned stress through E-beam lithography. The sample fabrication process, film, stress distribution, and magnetic domain structures are indicated from left to right. Reproduced with permission.<sup>[113]</sup> Copyright 2021, American Chemical Society.

Yang et al.<sup>[109]</sup> fabricated Ta/CoFeB/TaO<sub>x</sub>/MgO/Ta films on bendable mica substrates and observed that the density of the stripe domains increased and the magnetic bubble domains decreased upon convex bending of the substrate as the tensile strain in the state decreased the PMA and DMI strengths. These findings provide insight into novel storage devices with high density and power conservation.

#### 2.2.4. Stress/Strain Modulation of the Magnetic Domains

Magnetic domains are formed as the basic elements of the magnetic microstructure of a magnetically ordered material to minimize the total energy. Understanding the evolution of magnetic domains under mechanical stress is crucial for comprehending the intrinsic magnetic interactions of magnetic materials and enhancing the performance of flexible spintronic devices. Peng et al.<sup>[110]</sup> and Dai et al.<sup>[111]</sup> investigated the magnetic domain evolution by performing MFM measurements under varying strain states. Their research revealed that the magnetic domains of FeCoSiB and FeGa films align parallel to the direction of stress. As tensile stress increases, the contrast of the domain pattern weakens, and eventually, disappears at a large tensile stress, as shown in **Figure 9a**. Karboul–Trojet et al.<sup>[112]</sup> fabri-

cated NiFe thin films on flexible PI substrates that naturally displayed a stripe domain structure. They observed that while applying a saturating magnetic field eliminated the stripe domains, additional uniaxial tensile stress regenerated them. By leveraging the strain modulation of magnetic domain structures, Zhang et al.<sup>[113]</sup> achieved programmable magnetic domains through periodic nano-trenches patterned on PMMA using electron beam lithography (**Figure 9b**). This method of modulating the distribution of magnetic domains through microscopic stress patterning offers valuable insights for the design of nanoscale spintronic devices.

#### 2.2.5. Strategies for Enhancing the Stress/Strain Stability of Magnetization Direction

From the previous sections, the magnetic properties of flexible magnetic films are sensitive to mechanical stress, which may deteriorate the performance of flexible magnetoelectronic devices. Therefore, exploring methods for stabilizing the magnetic properties of flexible magnetic films for the preparation of high-performance flexible devices is imperative. Previous studies identified several strategies that could mitigate the adverse effects of mechanical stress on MA, such as depositing films with

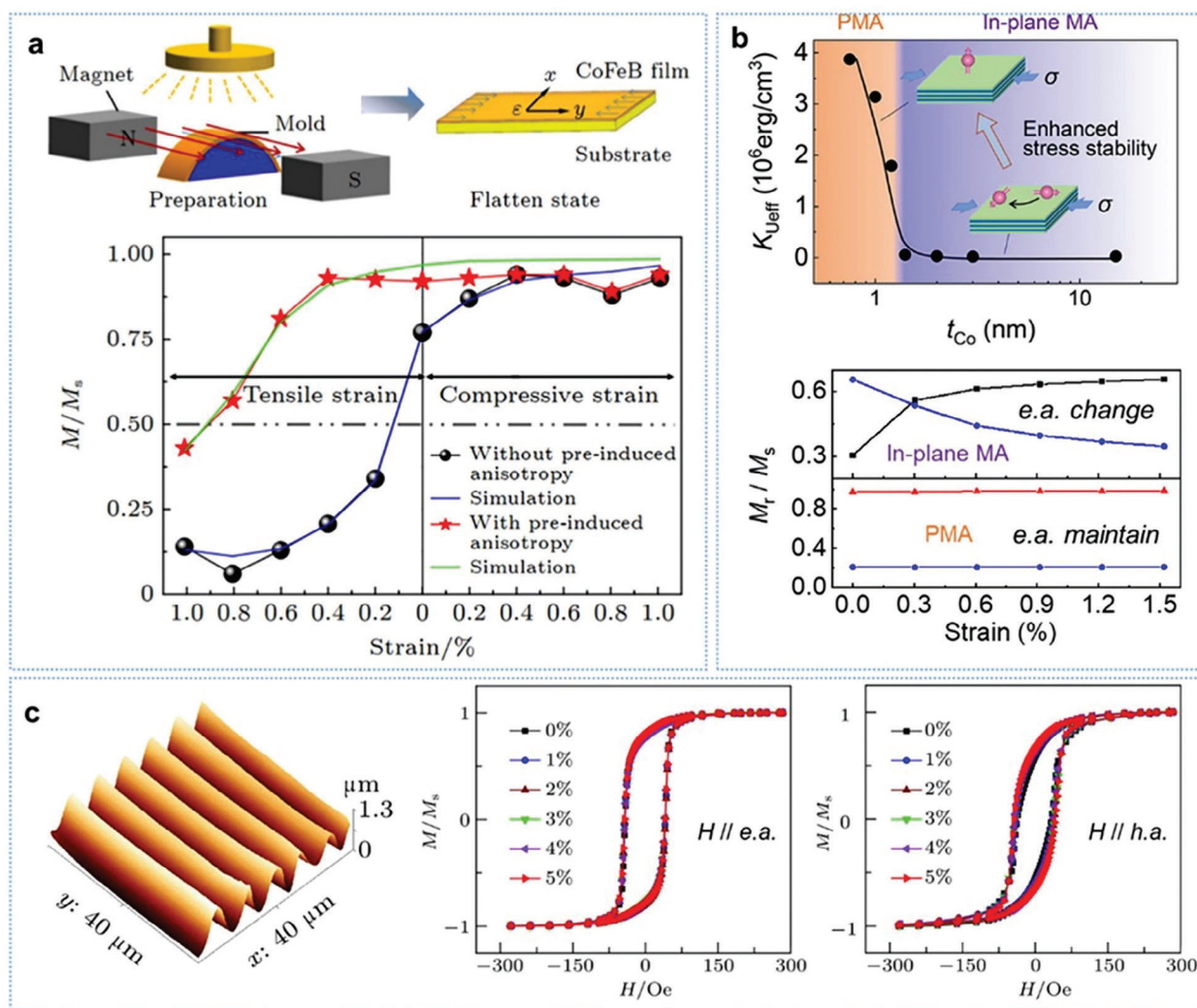


**Figure 10.** Strategies for enhancing the strain stability of magnetic orientation in flexible magnetic films. a) Film growth under pre-strain and magnetic fields. The easy axis of the films obtained is stable at a tensile strain of 0.4%, whereas that of normally grown films turns into the hard axis at a strain of 0.2%. Reproduced with permission.<sup>[115]</sup> Copyright 2017, AIP Publishing. b) Ultra-thin film growth with enhanced perpendicular MA. In the case of films with in-plane MA, the easy axis changes when a strain of  $\approx 0.3\%$  is applied, whereas for films with strong PMA, the easy axis maintains a strain of over 1.5%. Reproduced with permission.<sup>[40]</sup> Copyright 2023, American Chemical Society. c) Evolution of the magnetic properties of  $\text{Fe}_{10}\text{Co}_{90}$  films with periodically wrinkled structures upon tensile strain. Reproduced with permission.<sup>[119]</sup> Copyright 2020, IOP Publishing.

enhanced initial MA and releasing the strain through structural design.

Dai et al.<sup>[114]</sup> proposed a pre-strained deposition method to induce uniaxial anisotropy in flexible FeGa films. In this method, films were deposited on substrates attached to molds with curved surfaces. As the films flattened after growth, strain was generated, which induced an easy axis that could be maintained upon mechanical deformation. Qiao et al.<sup>[115]</sup> deposited CoFeB magnetic films on a bent substrate using a magnetic field perpendicular to the pre-strain. The coupling between the stress and magnetic fields enhanced the strength and stability of MA under stress (Figure 10a). The remanence ratio of the films with pre-induced anisotropy decreased from 0.92 to 0.43 within 1% tensile strain, whereas films lacking pre-induced anisotropy exhibited a reduction from 0.77 to 0.14 in the remanence ratio under 1% tensile strain. This observation underscores the stress stabil-

ity of MA in films deposited under both pre-strain and magnetic field conditions. Li et al.<sup>[40]</sup> proposed that strong PMA can enhance the stability of MA under in-plane stress. They conducted an experiment where Ta/Pt/[Co/Pt]<sub>4</sub> multilayers were deposited on PVDF and uniaxial compressive stress was applied by cooling the sample owing to the anisotropic thermal expansion of PVDF. As shown in Figure 10b, for [Co(1 nm)/Pt]<sub>4</sub> multilayers with strong PMA, the squareness ratio remained constant under compressive stress as high as 3.1 GPa, indicating excellent stress stability. However, for [Co(2 nm)/Pt]<sub>4</sub> multilayers with in-plane MA, the remanence ratio along the easy axis decreased from 0.64 to 0.22 under compressive stress.

Magnetic thin films with PMA hold significant potential in the development of magnetic sensors, memories, and logic devices with low energy consumption and high thermal stability. Recently, flexible PMA spin valves have garnered considerable

attention in various applications. For example, Hassan et al.<sup>[116]</sup> fabricated high-quality Co/Ni-based PMA spin valves with a sizable GMR ratio (up to 4.4%) on flexible polymer tapes. The properties of these samples remained robust even when subjected to bending at a curvature of  $0.4 \text{ mm}^{-1}$ , allowing for potential applications in wearable electronics, soft robotics, and biomedicine. Further, they highlighted the role of the buffer and capping layers in terms of different interdiffusion mechanisms at the interface between metallic layers, ultimately achieving a maximized GMR ratio by employing platinum group metals as the buffer layer and Cu as the capping layer. Matsumoto et al.<sup>[117]</sup> fabricated a flexible Pd/Co-based spin valve structure with in-plane free and out-of-plane fixed layers. They discovered that by applying a %-order biaxial tensile strain to the substrate, the magnetization in the free layer shifted from in-plane to out-of-plane orientation. This resulted in a significant and reversible change in the shape of the magnetoresistance curve, suggesting potential applications as a strain sensor or pressure detector. Makushko et al.<sup>[118]</sup> proposed the utilization of flexible PMA Co/Pd-based spin valves as magnetoreceptors for momentary and permanent (latching) switches. These switches maintained their performance even when bent to a radius of less than 3.5 mm and after repetitive bending for hundreds of cycles. They integrated these flexible switches in on-skin interactive electronics and demonstrated their effectiveness as touchless human-machine interfaces that are energy-efficient and insensitive to external magnetic disturbances.

Further, proper structural design is crucial in enhancing the stretching capability of flexible magnetic films. The release of stress in these films under deformation is essential for their performance. Among various structural patterns, the “wrinkled structure” is widely utilized in releasing the strain (thus stress) of magnetic films. The typical process of depositing magnetic films with wrinkles on flexible substrates is as follows: an amount of uniaxial stretching deformation (pre-stretch) is applied to the elastic substrates (for example, PDMS), the magnetic films are deposited on the pre-stretched elastic substrates, and finally, the wrinkle structure in the films is generated after releasing the pre-strain. This wrinkle structure results from the significant difference in Young’s modulus between the elastic substrate and magnetic film. Zhang et al.<sup>[44]</sup> proposed a method for enhancing the MA of flexible magnetic films. The process involved depositing a buffer layer onto pre-stretched elastic substrates, releasing the pre-strain to form a wrinkled structure, and then, depositing the magnetic films on the wrinkled structure. This innovative technique significantly enhanced the MA energy of FeGa films, increasing it by  $\approx 50$  times, which was beneficial for their stress stability. Zhao et al.<sup>[119]</sup> deposited  $\text{Fe}_{10}\text{Co}_{90}$  films onto wrinkled PDMS. They observed that the remanence ratio and coercivity along the easy axis remained constant even under a 5% tensile bending strain (Figure 10c). Moreover, they observed that oblique deposition could further enhance the MA of wrinkled magnetic films.<sup>[120]</sup>

### 3. Flexible Magnetosensitive Sensors

This section explores some widely used flexible magnetosensitive sensors, such as Hall, magnetoresistive (MR), and magnetoelectric sensors. We will delve into the working principles, preparation methods, and performance of the sensors.

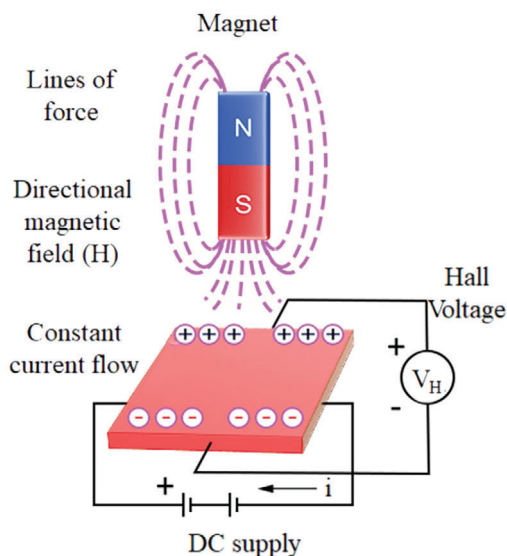


Figure 11. Schematic of a Hall sensor.

#### 3.1. Flexible Hall Sensors

Hall sensors utilize the Hall Effect, named after Edwin Hall, who discovered it in 1879. This effect occurs when a current-carrying conductor or semiconductor is placed in a magnetic field, as shown in Figure 11. The interaction between the current and magnetic field generates a voltage (Hall voltage) perpendicular to both the current and magnetic field as follows:  $V_H = \frac{I_x B_z}{n t e}$ , where  $I$  represents the current,  $B$  represents the magnetic field,  $n$  represents the carrier concentration, and  $t$  represents the thickness of the sensor. The generated Hall voltage is measured to determine the strength of the magnetic field. The sensitivity of a Hall sensor, which refers to the Hall voltage per unit magnetic field, is a crucial parameter for applications requiring precise magnetic field measurements.

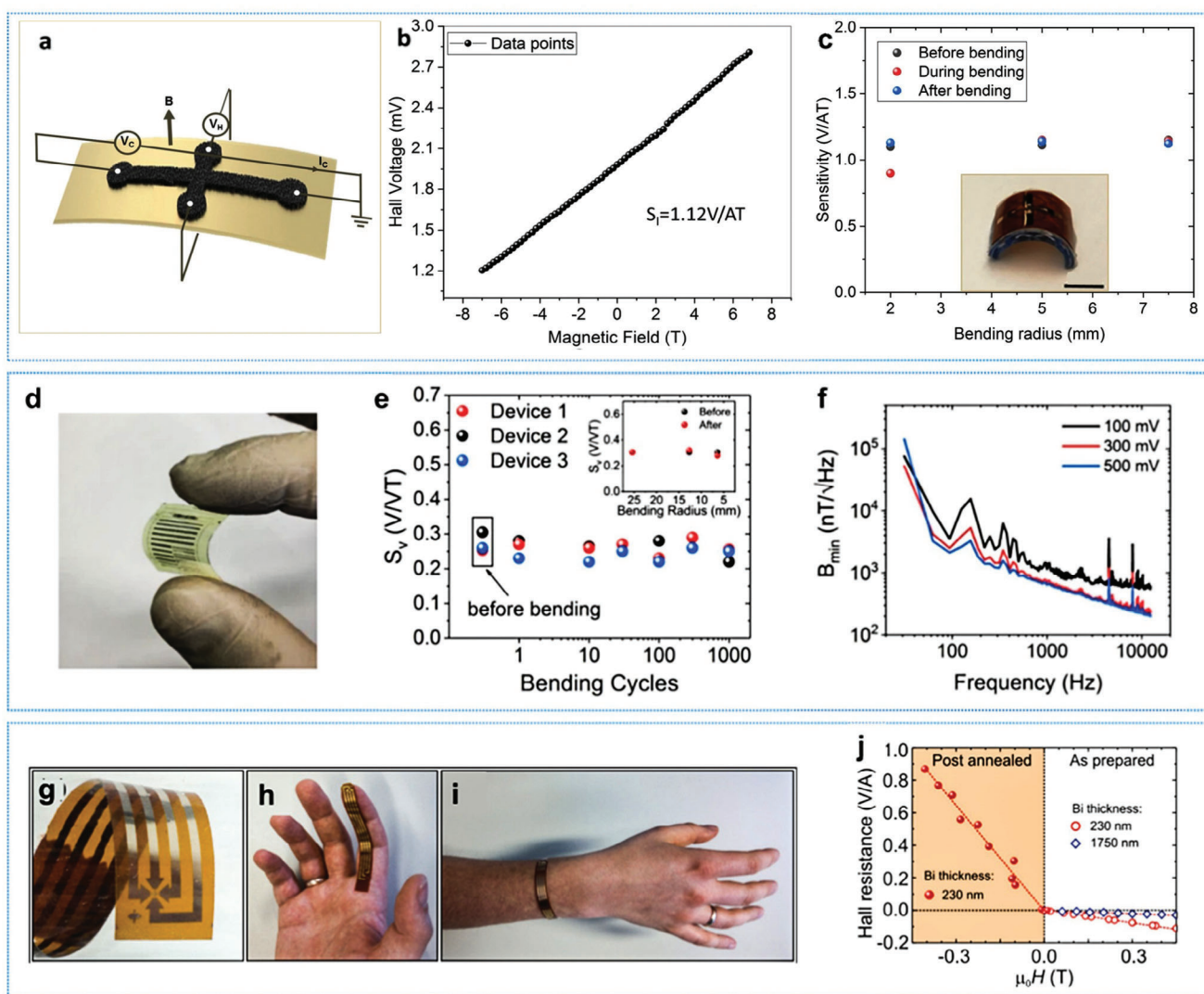
Flexible Hall sensors, made from materials, such as graphene, bismuth, and permalloys, have emerged as essential components in various domains owing to their high sensitivity, flexibility, and cost-effectiveness. The structures and performances of widely utilized Hall sensors are listed in Table 3. The high carrier mobility, low sheet carrier density, low-temperature dependence, atomic thinness, and mechanical flexibility of graphene make it an excellent material for flexible substrates. This enables

Table 3. Structure and performance of widely used hall sensors.

Material	Substrate	Sensitivity [V AT <sup>-1</sup> ]	Bending radius [mm]	Ref.
Graphene	Kapton	1.12	5	[121]
Graphene	Polyimide	800	6.4	[122]
Graphene	Kapton	79	5	[196]
Bismuth	Polyimide/polyether ether ketone	2.3	6	[124]
Bismuth	Polyether ether ketone	2.3	5	[125]

the realization of highly sensitive flexible Hall sensors<sup>[121,122]</sup> (Figure 12a–f). Kaidarova et al.<sup>[121]</sup> utilized laser scribed graphene to develop a flexible Hall sensor that provided a linear response to a magnetic field with a normalized sensitivity of  $\approx 1.12 \text{ V A}^{-1} \cdot \text{T}^{-1}$ , as shown in Figure 12b. The sensors also exhibited a low constant noise voltage floor of  $\approx 50 \text{ nV per } \sqrt{\text{Hz}}$  for a bias current of  $100 \mu\text{A}$  at room temperature. The sensors offer a unique combination of high bending flexibility, durability, and an operating temperature of up to  $400 \text{ }^\circ\text{C}$ . Graphene-based Hall sensors exhibit exceptional performance in sensitivity, linearity, resolution, and signal-to-noise ratio.<sup>[123]</sup> However, the high cost and complex synthesis of graphene have hindered its widespread commercial adoption. A promising alternative is bismuth thin-film-based Hall sensors fabricated on PI substrates<sup>[124,125]</sup> (Figure 12g–n).

Melzer et al.<sup>[124]</sup> fabricated highly flexible bismuth Hall sensors on polymeric foils with a sensitivity of  $-2.3 \text{ V A}^{-1} \cdot \text{T}^{-1}$ . These sensors could be bent around the wrist or placed on a finger to enable interactive pointing devices that visualized the relative position of the finger with respect to a magnetic field, offering unique feedback element applications for wearable electronics (Figure 12g–j). Mönch et al.<sup>[125]</sup> designed a flexible bismuth-based Hall sensor that was only  $80 \mu\text{m}$  thick, with a sensitivity of  $-230 \text{ mV A}^{-1} \cdot \text{T}^{-1}$ . The sensor could be mounted on curved surfaces with a radius as small as  $5 \text{ mm}$  without compromising its performance. These sensors exhibited voltage- and current-normalized sensitivities that could be compared with those of rigid silicon-based Hall sensors, demonstrating the feasibility of flexible substrates without compromising the sensor



**Figure 12.** Common flexible Hall sensor structures and their performances. a) Optical photo of a graphene flexible Hall sensor based on Kapton.<sup>[121]</sup> b,c) Sensor response to magnetic fields and sensitivity under different bending conditions.<sup>[121]</sup> Copyright 2021, Springer Nature with a Creative Commons CC-BY license. d) Optical photo of a graphene flexible Hall sensor based on polyimide.<sup>[122]</sup> e,f) Sensitivity of the sensor under different bending conditions and sensor noise.<sup>[122]</sup> Copyright 2019, Springer Nature with a Creative Commons CC-BY license. g–i) Schematic of a flexible bismuth-based Hall sensor on polyimide with excellent flexibility.<sup>[124]</sup> j) Flexible Hall sensor response to magnetic field.<sup>[124]</sup> Copyright 2015, Wiley-VCH with a Creative Commons CC-BY license.

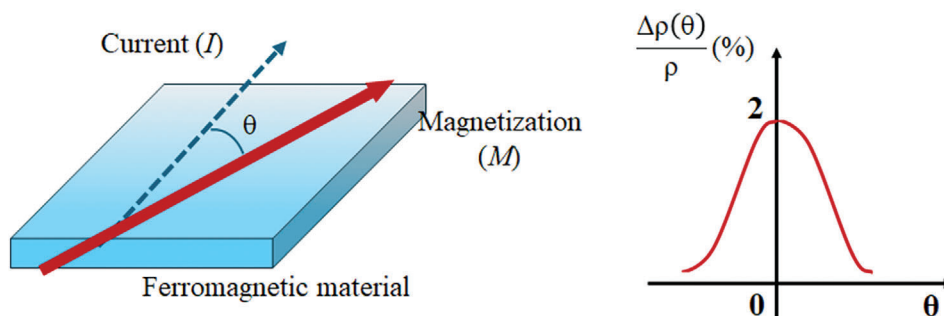


Figure 13. Schematic of an AMR sensor.

performance. These advancements expanded the applicability of Hall sensors in the field of flexible and wearable electronics.

### 3.2. Flexible Anisotropic Magnetoresistance Sensors

AMR, initially discovered in 1857 by William Thomas,<sup>[126]</sup> is a phenomenon that is based on the scattering behavior of electrons. This behavior varies significantly depending on the relative direction between the magnetization within the FM material and current, as shown in Figure 13. When the electrical current is aligned parallel to the magnetization of the FM material, the scattering cross-section is notably enhanced, resulting in maximum resistance. Conversely, the minimum resistance is observed in the case of the perpendicular alignment of the electrical current and magnetization. The AMR can be expressed as follows:

$$\rho(\theta) = \rho(90^\circ) + [\rho(0^\circ) - \rho(90^\circ)] \cos^2(\theta) \quad (1)$$

where  $\rho$  represents the longitudinal resistivity of the material and  $\theta$  represents the angle between the magnetization and current.

The planar Hall effect (PHE) characterizes the response of lateral voltage to a magnetic field and longitudinal current within the same plane.<sup>[127,128]</sup> Similar to the longitudinal voltage of the AMR, PHE exhibits high sensitivity in weak magnetic fields.

The primary materials utilized in AMR sensors are FM metals, such as Fe, Co, Ni, and their alloys, with the most common being the permalloy  $\text{Ni}_{81}\text{Fe}_{19}$ . Various studies on flexible AMR sensors are summarized in Table 4. To enhance the sensitivity, flexibility, and robustness of flexible AMR sensors, widely used methods involve spin-coating photosensitive anti-etching buffer layers onto flexible substrates.<sup>[129–131]</sup> These layers can reduce the surface roughness and promote the relaxation of surface strain

Table 4. Structure and performance of widely used AMR sensors.

Material	Substrate (thickness)	Sensitivity	Bending radius	Ref.
Py	PET (100 $\mu\text{m}$ )	$5 \text{ V T}^{-1}$	5 mm	[132]
Py	Mylar (2.5 $\mu\text{m}$ )	190% per T	20 $\mu\text{m}$	[81]
Py	PET (6 $\mu\text{m}$ )	$0.86 \text{ V T}^{-1}$	1 mm	[130]
NiFe/IrMn	Kapton/PDMS	$0.74 \mu\text{V Oe}^{-1}$	–	[133]
NiFe/IrMn	PDMS	$1.1 \mu\text{V Oe}^{-1}$	6.62 mm	[131]

caused by film growth. Granell et al.<sup>[130]</sup> developed a highly compatible novel flexible sensor on a flexible PET substrate by spin-coating an SU-8 layer. This sensor could detect weak magnetic fields ranging from 20 to 200 nT. Even when bent to a 1 mm radius, the sensor element maintained a sensitivity of  $0.86 \text{ V T}^{-1}$  with no signs of degradation during cyclic bending experiments (Figure 14a,b). Kim et al.<sup>[131]</sup> developed PHE sensors by depositing Ta/NiFe/IrMn/Ta thin films on flexible PDMS substrates with a parylene C polymeric buffer layer. The sensors exhibited reversible strain effects within a bending radius of 0.151  $\text{mm}^{-1}$  (Figure 14c-f). Wang et al.<sup>[132]</sup> fabricated flexible AMR sensors on PET substrates with a layer of photoresist, achieving a sensitivity similar to that of rigid substrates and excellent deformation stability. The electrical output remained consistent, even when the bending radius was reduced to 5 mm.

Advancements in flexible technology have eliminated the need for a buffer layer. A novel method involves printing AMR paste onto flexible substrates.<sup>[81]</sup> The printable paste is a composite material that comprises Py/Ta thin films embedded in an elastomeric matrix. The paste can be printed in ultrathin polymer foils (2.5  $\mu\text{m}$ ). The AMR sensor can detect magnetic fields below 1 mT and exhibits stable magnetoresistive characteristics even when mechanically bent with a bending radius of 20  $\mu\text{m}$  (Figure 14g-i). Ozer et al.<sup>[133]</sup> prepared a NiFe/IrMn bilayer structure on a double-layer Kapton/PDMS substrate, demonstrating a stable response under repeated on/off experiments. Based on bending test results, the AMR sensor exhibited high sensitivity with  $0.74 \mu\text{V Oe}^{-1} \cdot \text{mA}^{-1}$ .

### 3.3. Flexible Giant Magnetoresistance Sensors

In 1988, Grünberg and Fert discovered the GMR effect; while, working independently. In the multilayer film structure comprising FM layer–nonmagnetic (NM) layers–FM layers, the electrical resistance is closely related to the magnetization direction of the thin FM film layers,<sup>[134–136]</sup> as shown in Figure 15. When the magnetization directions of the two magnetic layers are aligned in opposite directions, the resistance is significantly higher compared with when they are parallel. GMR can be defined as follows:  $\text{GMR} = (R_{\text{H}} - R_0) / R_0 \times 100\%$ , where  $R_0$  represents the resistance of the sample at zero magnetic field and  $R_{\text{H}}$  represents the resistance of the sample at saturation magnetic field. The most flexible GMR magnetic sensors are based on two structures: multilayers<sup>[43,78,137–141]</sup> and spin valve.<sup>[41,45,142,143]</sup> The

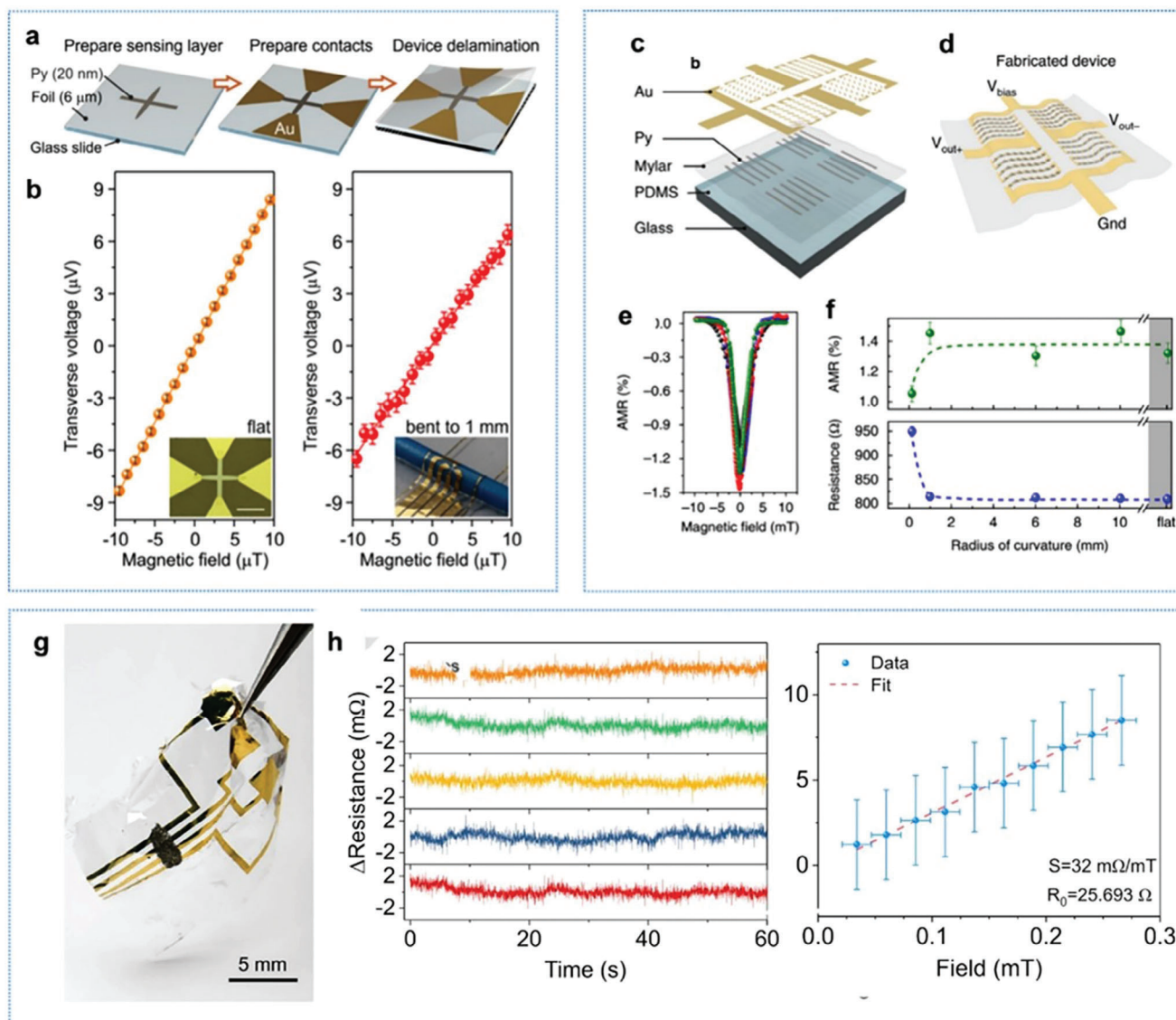


**Figure 14.** a,b) Schematics of the fabrication process of a flexible PHE sensor and magneto-electrical characterization of flexible PHE sensors in the flat state and when bent to 1 mm.<sup>[130]</sup> Copyright 2019, Springer Nature with a Creative Commons CC-BY license. c–f) Fabrication process and properties of the e-skin compass. Reproduced with permission.<sup>[29]</sup> Copyright 2018, Springer Nature. g–i) Printed AMR sensor and AMR response of the deposited Py/Ta film measured on the wafer.<sup>[81]</sup> Copyright 2021, Springer Nature with a Creative Commons CC-BY license.

representative studies on flexible GMR sensors are summarized in **Figure 16** and **Table 5**.

The GMR multilayer structure typically comprises alternating layers of magnetic and nonmagnetic materials. The GMR effect arises from the interlayer AFM coupling between two FM material layers separated by NM layers. To mitigate the impact of substrate roughness on performance, Chen et al.<sup>[139]</sup> employed buffer layers deposited on a substrate, resulting in a 115–200% enhancement in GMR values compared with those without buffer layers. The prepared thin films could withstand a tensile strain of 2.7%; while, maintaining resistance and magnetoresistive performance after 1000 bending cycles with a radius of  $\approx 22$  mm (Figure 16a). Oliver et al.<sup>[43]</sup> fabricated GMR multilayers with a (Co/Cu)<sub>50</sub> structure on an elastic PDMS membrane,

achieving GMR values exceeding 50%. By inducing wrinkling in the composite film through thermal strain on the elastic PDMS membrane, they provided a tensile strain of 4.5% (Figure 16b). In addition to enhancing the tensile performance through thermal pre-strain, they enhanced the tensile performance of GMR multilayer magnetic sensors from 4% to 30% by utilizing mechanical strain-induced pre-strain<sup>[140]</sup> (Figure 16c). Further, they printed GMR sensors on an FPC board, resulting in optimized magnetic sensors that exhibited up to a 37% change in electrical resistance in the presence of a magnetic field with a maximum sensitivity of  $0.93 \text{ T}^{-1}$  at 130 mT (Figure 16d)<sup>[78]</sup>. To achieve better tensile properties, they replaced PDMS with highly elastic PET films as substrates, achieving a tensile strain of up to 270% and withstanding 1000 cycles of tensile deformation<sup>[141]</sup> (Figure 16e).

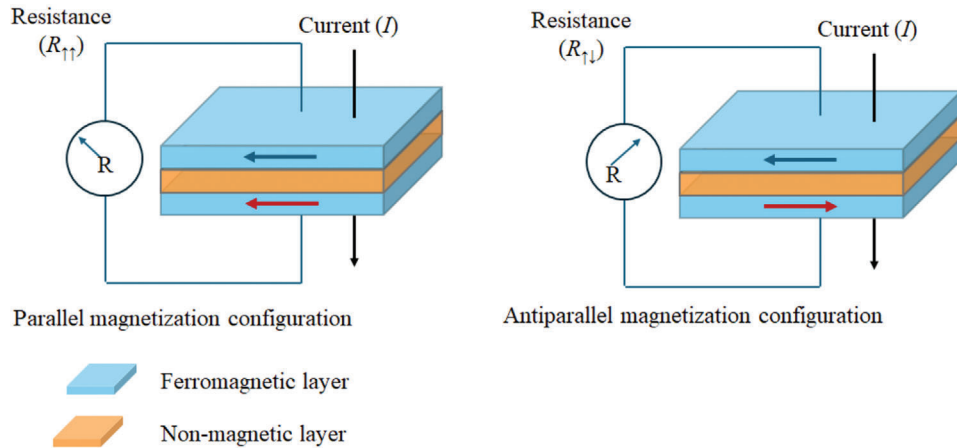


Figure 15. Schematic of a GMR sensor.

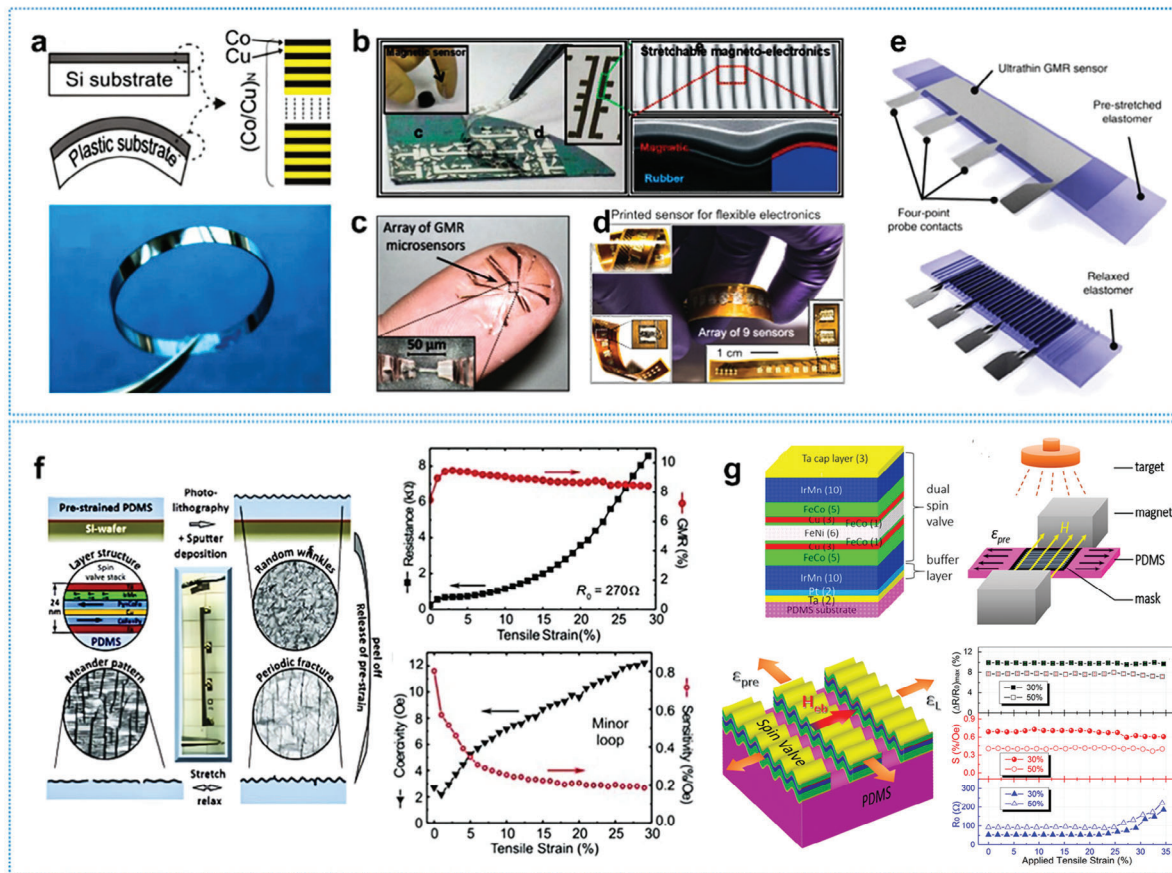


Figure 16. a) Schematic and photographic image of  $(\text{Co/Cu})_N$  MLs deposited on Si and flexible substrates.<sup>[139]</sup> Copyright 2008, Wiley-VCH with a Creative Commons CC-BY license. b) Optics and morphology of the stretchable magnetic sensor. Reproduced with permission.<sup>[43]</sup> Copyright 2011, American Chemical Society. c) Transferred microsensors conforming to the soft and curved surface of a fingertip.<sup>[140]</sup> Copyright 2008, Wiley-VCH with a Creative Commons CC-BY license. d) Application of the GMR paste through regular brush painting to a flexible printed circuit board to realize an array of printed GMR sensors for flexible electronics. Reproduced with permission.<sup>[78]</sup> Copyright 2015, Wiley-VCH. e) Stretchable magneto-electronics. A multilayer GMR element on ultrathin PET is laminated face down onto pre-stretched elastomer relaxation in out-of-plane wrinkling of the sensor foil and re-stretching (bottom).<sup>[124]</sup> Copyright 2015, Wiley-VCH with a Creative Commons CC-BY license. f) Fabrication process of stretchable magnetic sensors with random wrinkling and periodic fracture of the spin valve stack.<sup>[41]</sup> Copyright 2015, Wiley-VCH with a Creative Commons CC-BY license. g) Layer structure of the dual spin valve and applied tensile strain dependence of the GMR ratio  $(\Delta R/R_0)_{\text{max}}$  (squares), magnetic field sensitivity  $S$  (circles), and zero-field resistance  $R_0$  (triangles) for SVR-30% (solid symbols) and SVR-50% (open symbols). The uniaxial tensile strain from 0 to 35% was applied along the ribbons. Reproduced with permission.<sup>[45]</sup> Copyright 2016, American Chemical Society.

**Table 5.** Structure and performance of widely used GMR sensors.

Type	Material	Substrate (thickness)	GMR ratio	Sensitivity	Bending radius/tensile strain	Ref.
GMR multilayers	Co/Cu multilayers	Photoresist + polyester	≈48%	–	22 mm/2.7%	[139]
	Co/Cu multilayers	PDMS (40 μm)	50%	–	–/4.5%	[43]
	Py/Cu multilayers	PDMS (60 μm)	57%	220%/T	–/30%	[140]
	Co/Cu multilayers	PET (1.4 μm)	57.8%	220%/T	0.003 mm/270%	[141]
	Co/Cu multilayers	FPC board	37%	93%/T	12 mm	[78]
GMR spin valve		PI	8.6%	$S = (\Delta R/R)/\Delta\epsilon = 2.2$	≈2.5%	[142]
	PtMn/Co <sub>25</sub> Fe <sub>25</sub> /Ru/Co <sub>25</sub> Fe <sub>25</sub> /Cu/Co <sub>50</sub> Fe <sub>50</sub>					
	Ta/FeGa/FeCo/Cu/FeCo/IrMn/Ta	PET	5.9%	$S = (\Delta R/R)/\Delta\epsilon = 7.2$	1.8%	[143]
	Ta/IrMn/Py/CoFe/Cu/CoFe/Py	PDMS	≈9%	0.2% per Oe	29%	[41]
	Ta/IrMn/CoFe/Cu/CoFe/Py /CoFe/Cu/CoFe/IrMn/Pt/Ta	PDMS	9.9%	0.69% per Oe	>50%	[45]

The GMR spin valve structure primarily comprises magnetic free layers, NM spacer layers, FM pinning layers, and AFM pinning layers. The GMR effect is influenced by the relative orientations of the free and pinned layers. In an attempt to prevent a sharp decrease in the GMR ratio, Liu et al.<sup>[143]</sup> deposited a spin valve structure on a PET substrate with composite-free layers of FeGa/FeCo. The FeGa alloy exhibited magnetostrictive properties that enhanced the strain sensitivity of the film. Melzer et al.<sup>[41]</sup> introduced a method for fabricating highly elastic GMR spin valve sensors on PDMS substrates by employing a predetermined periodic fracturing mechanism and random wrinkling. The device maintained a GMR of 7% under 29% tensile strain (Figure 16f). Li et al.<sup>[45]</sup> deposited thin films with a double-spin valve structure on a flexible PDMS substrate using DC sputtering. The fabricated device featured a strain-relief structure that combined periodic wrinkles and parallel ribbons, accommodating biaxial strain during stretching operations, thereby mitigating the impact of the residual strain on the GMR performance. Under a 30% pre-strain condition, they achieved a GMR ratio of 9.9% and a magnetic field sensitivity of up to 0.69% per Oe. The resistance and magnetic field sensitivity of the device were maintained after 500 cycles of stretching, making it suitable for applications in smart electronic skin or wearable electronic devices that adhere to the body (Figure 16g).

To further improve the sensor performance, particularly in terms of immunity to electromagnetic interference, flexible sensing elements should be incorporated into in-field signal conditioning electronics.<sup>[144,145]</sup> Previously, it was assumed that the solution to this problem was to combine high-performance GMR sensorics with flexible, thin Si membranes capable of accommodating integrated CMOS circuitry.<sup>[146]</sup> However, research has shown that flexible GMR sensors can also be conditioned using flexible inorganic and organic electronics. For example, Münzenrieder et al.<sup>[147]</sup> demonstrated a fully integrated magnetosensory system on a 50 μm thick polyimide foil. This system comprised a differential GMR sensing element arranged in a Wheatstone bridge configuration, an operational amplifier based on 16 indium–gallium–zinc–oxide thin-film transistors (TFTs), and a high-current output amplifier TFT operated as a class. A power amplifier with an open drain output provided the maximum adaptability to different loads (Figure 17a). The in-

tegrated flexible amplifiers exhibited outstanding performance, such as a remarkable amplification of 48.6 dB, unity gain frequency of up to 200 kHz, gain-bandwidth product of 54 MHz, and minimum bending radius of 5 mm. With this remarkable performance, the researchers demonstrated various applications of the integrated magnetosensory system, such as magnetically activated energy-efficient sensors and switches. Kondo et al.<sup>[148]</sup> demonstrated an imperceptible magnetic sensor matrix system comprising an array of magnetoresistance sensors, a bootstrap organic shift register as the active matrix driver, and organic signal amplifiers (Figure 17b). The utilization of organic amplifiers in the system resulted in high magnetic sensitivity, whereas the shift register allowed for real-time mapping of 2D magnetic field distribution. This technology can be utilized in applications, such as e-skins, soft robotics, and biomedical science.

### 3.4. Flexible Tunneling Magnetoresistance Sensors

Initially discovered by Julliere<sup>[149]</sup> in the MTJ sandwiching an extremely thin insulator layer (typically on the order of nanometers) between two FM layers, TMR demonstrates a significant change in the tunneling current when the relative orientations of the magnetizations in the two FM layers change. The schematic of the TMR sensor is shown in Figure 18. An ideal flexible TMR device should possess characteristics, such as being lightweight, having good mechanical stretchability, compatibility, and portability. However, the development of TMR devices on flexible organic substrates is challenging. Overcoming the brittleness of inorganic metals is a primary obstacle. Another significant challenge involves addressing the reduced magnetoelectric performance of TMR thin films owing to the utilization of rougher flexible substrates and the fabrication processes involving heating, micromachining, and chemical etching. Some representative studies on flexible TMR sensors are summarized in Figure 19 and Table 6. The first flexible TMR sensor<sup>[71]</sup> was fabricated by spin-coating two layers of organic buffer materials to flatten the surface of the flexible substrate and grow large-area Co/Al<sub>2</sub>O<sub>3</sub>/Co MTJs on it. Compared with rigid Si/SiO<sub>2</sub> substrates, the spin-dependent tunneling properties of this flexible

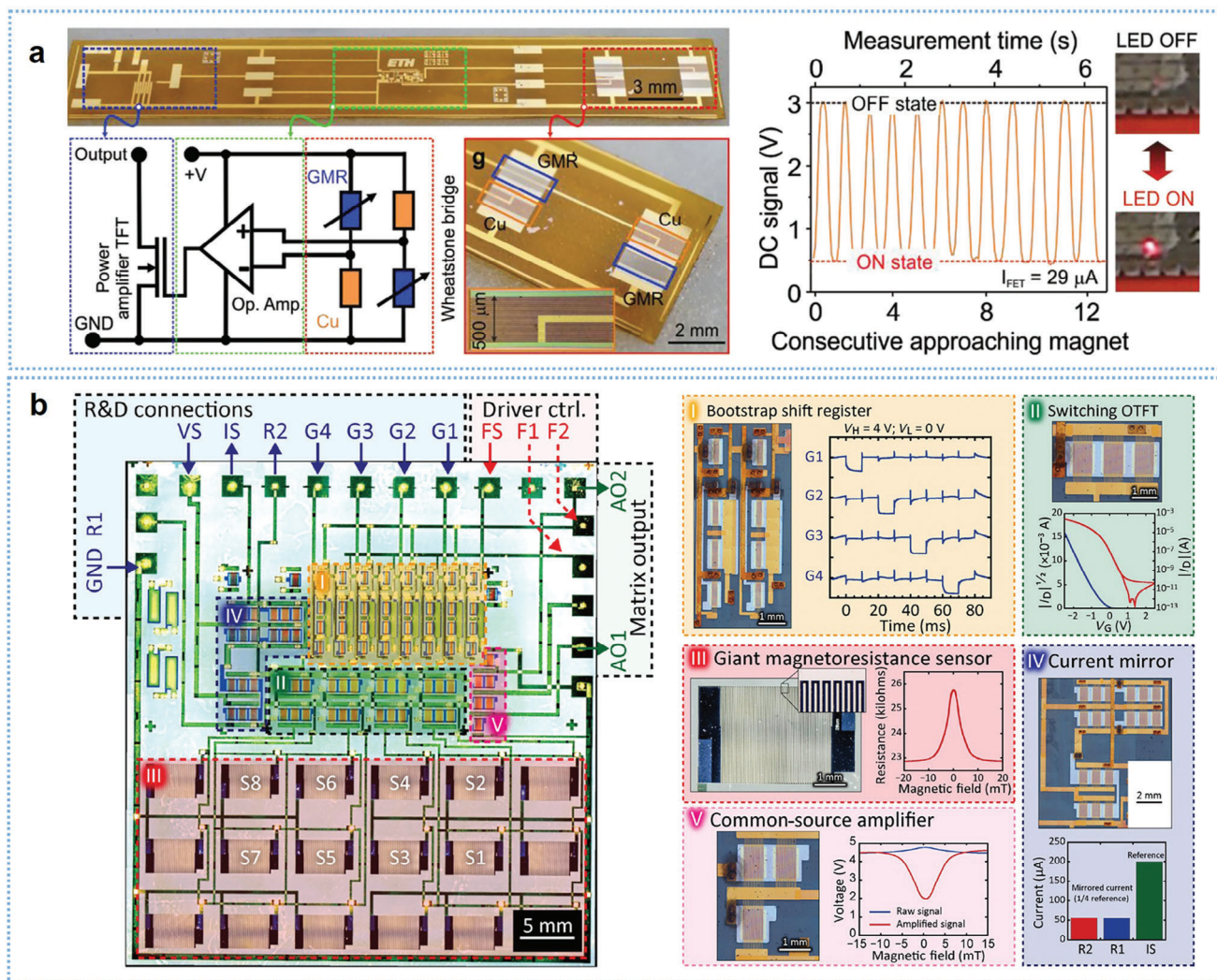


**Figure 17.** a) Integrated magnetosensory system on a polyimide foil, comprising a differential GMR sensing element arranged in a Wheatstone bridge configuration, operational amplifier, and output power amplifier. Output of the flexible integrated magnetosensory system as a magnetic switch.<sup>[147]</sup> Copyright 2016, Wiley-VCH with a Creative Commons CC-BY license. b) Construction of the imperceptible magnetosensory system with an area of  $50 \times 50 \text{ mm}^2$  along with the five main building blocks designed and implemented in imperceptible form and principal characteristics.<sup>[148]</sup> Copyright 2020, AAAS with a Creative Commons CC-BY license.

TMR sensor remained unchanged. When the bending strain exceeded 1%, corresponding to a bending radius of  $\approx 15 \text{ mm}$ , no cracks or electrical hot spots were generated owing to mechanical stress. Bedoya-Pinto et al.<sup>[150]</sup> demonstrated that Kapton is a promising low-cost platform for flexible spintronic applications. The TMR thin films grown on Kapton exhibited magnetic transport properties of up to 12%, and these properties remained unaffected even when the substrate was bent (Figure 19a). Gaspar et al.<sup>[151]</sup> have shown that TMR multilayer films grown on polyimide display a magnetoresistive response exceeding 150%, with a sensitivity of up to  $250 \mu\text{V Oe}^{-1}$ . Notably, even when the bending radius was reduced to 5 mm, the performance was minimally impacted (Figure 19b). Ota et al.<sup>[152]</sup> observed an enhancement in the crystallization of CoFeB and MgO layers at higher temperatures. TMR could reach 200% at  $450 \text{ }^\circ\text{C}$ , demonstrating its stress tolerance. Amara et al.<sup>[153]</sup> fabricated a flexible TMR sensor on

a thinned silicon wafer, demonstrating high reliability and mechanical stress resistance. This sensor could withstand a bending radius as low as  $500 \mu\text{m}$  and over 1000 cycles without fatigue (Figure 19c).

### 3.5. Flexible Non-Saturating Large Magnetoresistance Sensors

Some materials exhibit non-saturating large magnetoresistance (LMR).<sup>[154–156]</sup> These materials can significantly expand the detection range of the external magnetic field. LMR effects are typically observed in semimetals, where linear band crossings occur at the Fermi energy, resulting in extremely high mobilities and low effective mass.<sup>[157]</sup> In semi-classical magnetotransport theory, the LMR phenomenon can be explained through the electron–hole resonance compensation mechanism. Based on the two-band

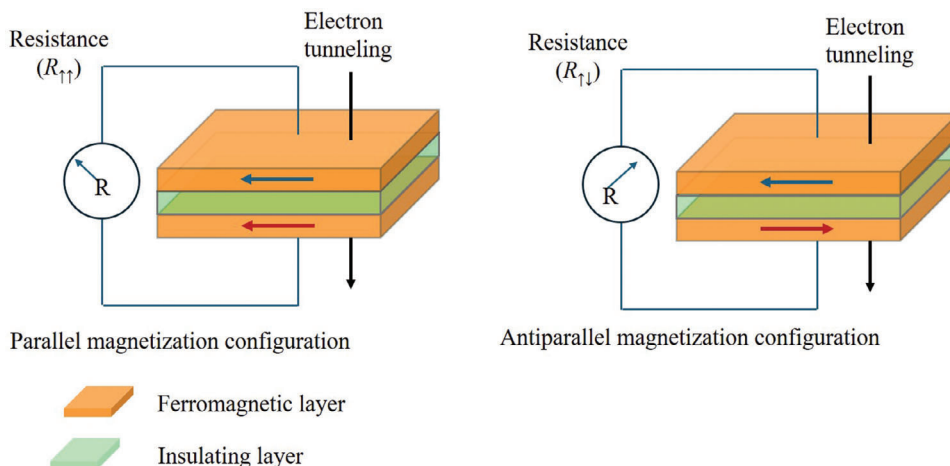


Figure 18. Schematic of a TMR sensor.

model, the conductivity tensor  $\sigma$  can be expressed in the complex representation as follows:

$$\hat{\sigma} = e \left[ \frac{n\mu}{(1+i\mu B)} + \frac{p\mu'}{(1-i\mu' B)} \right] \quad (2)$$

where  $e > 0$  represents the charge, whereas  $\mu$  and  $\mu'$  represent the electron and hole mobilities, respectively. The complex resistivity  $\rho$  represents the reciprocal of  $\sigma$ :

$$\hat{\rho} = \frac{1 + \mu\mu' B^2 + i(\mu - \mu') B}{e [n\mu + p\mu' + i(p - n)\mu\mu' B]} \quad (3)$$

If  $p = n$ , a non-saturating parabolic magnetoresistance can be observed. When charge neutrality is disrupted in semimetals (that is  $n \neq p$  as in most cases), the magnetoresistance will saturate at a specific magnetic field depending on the value of  $|n - p|$ . Bismuth is a well-known example of a material that falls into this category. Recently, Oliveros-Mata et al.<sup>[83]</sup> fabricated flexible bismuth-based sensors that exhibited the LMR effect at room temperature. They innovatively adopted printing technology to fabricate bismuth-based LMR sensors on various substrates, including ceramics, paper, and polymer foils. The sensors exhibited up to 146% resistance change at 5 T at room temperature, with a maximum resolution of 2.8  $\mu$ T. In addition, they displayed resilience to bending deformation for over 2000 bending cycles, making them suitable for potential applications in touchless interactive platforms.

### 3.6. Flexible Giant Magneto-Impedance Sensors

The giant magnetoimpedance (GMI) effect refers to the phenomenon in which soft magnetic materials exhibit significant sensitivity to changes in an externally applied magnetic field ( $H_{\text{ex}}$ ) when subjected to an alternating current ( $I_{\text{ac}}$ ) (Figure 20). This effect was first observed in 1992 in amorphous CoFeSiB wires, known for their low magnetic hysteresis, high sensitivity, and exceptional performance. The rate of change of the GMI effect un-

der the influence of an external magnetic field can be calculated as follows:

$$\frac{\Delta Z}{Z(\%)} = 100\% \times \frac{Z(H_{\text{ex}}) - Z(H_{\text{max}})}{Z(H_{\text{max}})} \quad (4)$$

where  $H_{\text{max}}$  represents the external magnetic field at saturation impedance.

The GMI effect is primarily attributed to the skin effect in soft magnetic materials at high frequencies.<sup>[158–162]</sup> The variation in current density from the surface to the interior is represented by the skin depth, calculated as follows:

$$\delta = \sqrt{2\rho/\omega\mu} \quad (5)$$

where  $\mu$  represents magnetic permeability,  $\rho$  denotes resistivity, and  $\omega$  represents the cyclic frequency of the current. The correlation between the magnetic permeability of the soft magnetic material and external magnetic field is the key factor driving the GMI effect.

The GMI effect is evident in FM materials, particularly in ultra-soft magnetic wires and strips of amorphous or nanocrystalline structures, such as permalloys and Co/Fe-based amorphous alloys (CoSiB, CoFeSiB, and CoFeMoSiB).<sup>[163]</sup> Representative studies on flexible GMR sensors are summarized in Figure 21 and Table 7.

For example, Fernandez et al.<sup>[164]</sup> demonstrated that nanostructured multilayers deposited onto a flexible polymeric substrate can yield an excellent GMI response. Their empirical analysis validated that multilayer magneto-impedance (MI) sensors, operating at 150 MHz, achieved an MI ratio of 110% along with a magnetic sensitivity of 22% per Oe.<sup>[164]</sup> Building upon this research, Agra et al.<sup>[165]</sup> scrutinized non-magnetostrictive multilayer films on Kapton substrates, revealing an MI ratio of 60% at a higher frequency of 0.45 GHz. Karnaushenko et al.<sup>[166]</sup> proposed a novel method based on strain engineering to realize arrays of on-chip-integrated GMI sensors equipped with pickup coils. They introduced a new photopatternable, thermally, and chemically stable polymer platform that enabled the self-assembly of planar NiFe/Cu/NiFe-based heterostructures into 3D tubular

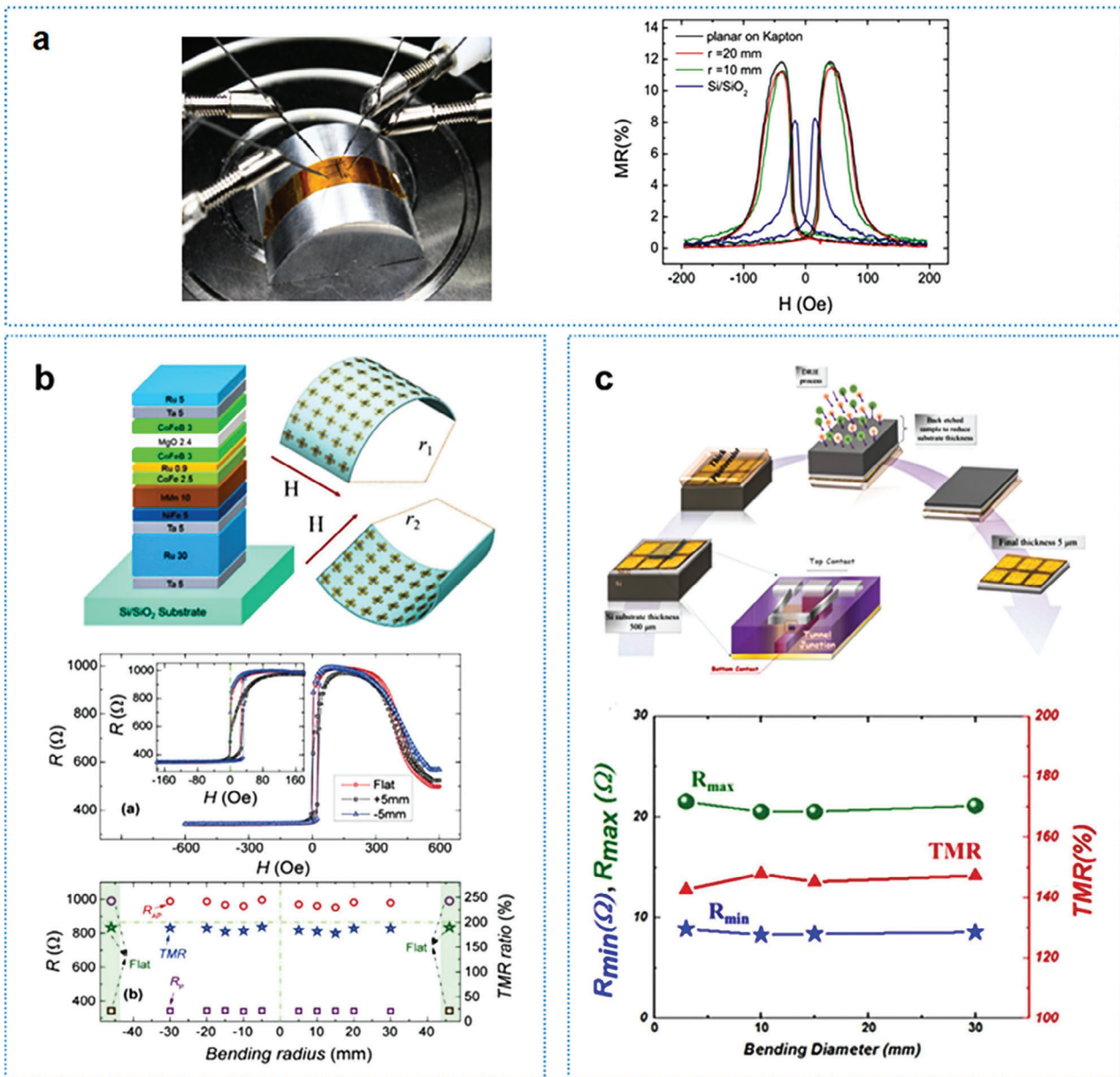


**Figure 19.** a) Schematic of the shadow mask-patterned MTJ and a picture illustrating device bending. Reproduced with permission.<sup>[150]</sup> Copyright 2014, AIP Publishing. b) Schematic of the fabrication process of flexible MgO-barrier MTJs and TMR rate in the flat configuration after several bending cycles. Reproduced with permission.<sup>[191]</sup> Copyright 2017, Springer Nature with a Creative Commons CC-BY license. c) Fabrication process flow of MTJ devices and coercive field, saturation, and remanent magnetizations of the MTJ stack on a flexible Si substrate measured using a vibrating sample magnetometer versus the bending diameter. Reproduced with permission.<sup>[153]</sup> Copyright 2018, Wiley-VCH.

architectures with GMI functionality. This self-assembly method enabled high-performance GMI arrays capable of measuring magnetic fields from 2 to 100 pT, with an  $\approx 100\%$  GMI change rate (Figure 21a–c). In addition, the sensing element could be positioned within a distance of less than 10 mm from the current element that generated the magnetic field. These advancements laid a solid foundation for the further development of CMOS-compatible GMI sensorics for magnetoencephalography applications. Subsequently, Li et al.<sup>[167]</sup> performed deflection measurements on a flexible MI sensor composed of a

$\text{Ni}_{80}\text{Fe}_{20}/\text{Cu}/\text{Ni}_{80}\text{Fe}_{20}$  trilayer on Kapton substrates. Deflection measurements were conducted on the MI sensor through a flexible microstrip transmission line over a wide range of frequencies (0.1–3 GHz). Notably, these sensors retained a significant MI ratio of up to 90% and exhibited magnetic sensitivities of up to 9.2% per Oe. This feature makes the device suitable for wireless applications, particularly in scenarios with small antenna sizes and compliance with GHz frequency regulations (Figure 21d–f).

Recently, CoFe-based amorphous wires have garnered significant attention owing to their excellent mechanical, magnetic,

**Table 6.** Structure and performance of widely used TMR sensors.

Material	Substrate (thickness)	TMR ratio	Sensitivity	Bending radius/strain	Ref.
Co/Al <sub>2</sub> O <sub>3</sub> -based Co/Al <sub>2</sub> O <sub>3</sub> /Co	Gel-film (300 μm)	12.5%	–	15 mm/1%	[71]
Co/Al <sub>2</sub> O <sub>3</sub> /NiFe	Kapton	12%	–	5 mm	[150]
[Ta/CuN] <sub>6</sub> /Ta/Ru/IrMn/Co <sub>70</sub> Fe <sub>30</sub> /Ru/Co <sub>40</sub> Fe <sub>40</sub> B <sub>20</sub> /MgO/Co <sub>40</sub> Fe <sub>40</sub> B <sub>20</sub> /Ta/NiFe/Ru/IrMn/Ru/Ta/Ru	PI	171%	250 μV per Oe	5 mm	[151]
Ta/CuN/Ta/CuN/Ta/Pt <sub>38</sub> Mn <sub>62</sub> /Co <sub>70</sub> Fe <sub>30</sub> /Ru/Co <sub>40</sub> Fe <sub>40</sub> B <sub>20</sub> /MgO/Co <sub>40</sub> Fe <sub>40</sub> B <sub>20</sub> /Ta/CuN/RuTa	Silicon (3–5 μm)	–	4.93% per Oe	0.5 mm	[153]
Ta/Ru/Ta/Ni <sub>81</sub> Fe <sub>19</sub> /Ir <sub>22</sub> Mn <sub>78</sub> /Co <sub>90</sub> Fe <sub>10</sub> /Ru/Co <sub>20</sub> Fe <sub>60</sub> B <sub>20</sub> /MgO/CoFeB/Ta/Ru	Silicon (14 μm) Kapton	190%	–	2 mm	[191]
Ta/Ru/Ta/Co <sub>20</sub> Fe <sub>60</sub> B <sub>20</sub> /MgO/Co <sub>20</sub> Fe <sub>60</sub> B <sub>20</sub> /Ta/Ru	UPILEXVR S50	200%	–	1.6%	[152]
CoFeB/MgO/CoFeB	PET (188 μm)	300%	–	1%	[70]

microwave, and GMI properties. Nabias et al. proved that amorphous wires still exhibited excellent GMI effects under bending, allowing for accurate magnetic field measurements under such conditions<sup>[168]</sup> (Figure 21g,h). For example, Jiang et al.<sup>[169]</sup> systematically investigated the effect of Cu substitution and fabrication characteristics on the variations of surface microstructures. Their findings correlated with the mechanical and GMI properties of the melt-extracted CoFe-based wires. Further, they achieved a GMI ratio of up to  $700 \pm 5\%$  with the amorphous wire operating at  $\approx 7\%$  strain.

### 3.7. Flexible Magnetolectric Sensors

Magnetolectric (ME) sensors leverage the interaction between magnetic and electric properties inherent in specific materials, known as the ME effect. This effect manifests as a coupling mechanism where a magnetic field can induce electric polarization within the material and vice versa. Typically, these sensors are designed in a layered configuration, combining magnetostrictive and piezoelectric materials (Figure 22). The magnetostrictive layer experiences mechanical strain under a magnetic field, which is then converted into an electric signal by the adjacent piezoelectric layer. The output voltage of the sensor can be determined as follows:

$$V = \alpha_{ME} H \quad (6)$$

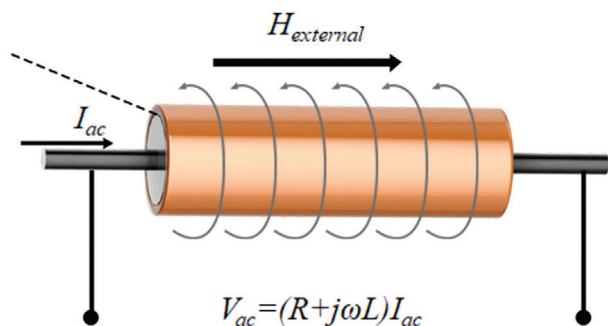


**Figure 20.** Schematic of a GMI sensor.

where  $\alpha_{ME}$  represents the ME coupling coefficient, determined by the material properties and structural parameters of the sensor, and  $H$  represents the magnetic field strength. Therefore, the voltage output of a sensor is solely dependent on the magnitude of the external magnetic field. Magnetic field measurements are achieved by monitoring the voltage output of the sensor.

Extensive studies on piezoelectric materials have been conducted to advance the field of flexible ME sensors. Among these materials, PVDF<sup>[170]</sup> and its copolymers have emerged as standout candidates owing to their exceptional piezoelectric attributes. In addition, magnetostrictive materials play a crucial role in ME sensors by converting changes in the magnetic field into deformation, thereby inducing corresponding strains in the piezoelectric material (Figure 23a,b). One notable magnetostrictive material, Metglas, has been integrated with piezoelectric constituents, such as PVDF; although, its limited flexibility makes it suitable for specific applications. Chlahawiet et al.<sup>[171]</sup> employed silk-screen printing of piezoelectric PVDF ink on a flexible magnetic Metglas substrate, achieving an impressive ME voltage coefficient of  $84.5 \text{ mV cm}^{-1} \cdot \text{Oe}^{-1}$  (Figure 23c,d). The response of the sensor to magnetic fields was linear, with a sensitivity of  $503.3 \text{ V T}^{-1}$  and a correlation coefficient of 0.9994. Yang et al.<sup>[172]</sup> combined piezoelectric  $\text{Pb}(\text{Zr}_{0.52}\text{Ti}_{0.48})\text{O}_3$  thick films with Metglas foils to fabricate a flexible ME sensor. This sensor exhibited an ME coefficient of  $19.3 \text{ V cm}^{-1} \cdot \text{Oe}^{-1}$  at low frequencies and showed no fatigue-induced performance degradation after 5000 bending cycles (radii of  $\approx 1 \text{ cm}$ ) (Figure 23e,f).

A novel flexible ME sensor, based on electromagnetic induction, has garnered widespread attention. This sensor is composed of a pliable coil and magnet. When the sensor is deformed, the magnetic flux within the coil changes, leading to the generation of a corresponding voltage through electromagnetic induction. Zhang et al.<sup>[173]</sup> developed a unique flexible ME device using advanced methodologies, such as 3D-printed molds, Ecoflex substrates, gallium-based liquid metal, and strategically integrated magnetic plates. The detailed fabrication process of the device is shown in Figure 23g,h. Notably, the incorporation of a liquid metal provides unparalleled levels of flexibility and extensibility, pushing the boundaries of conventional sensor capabilities.

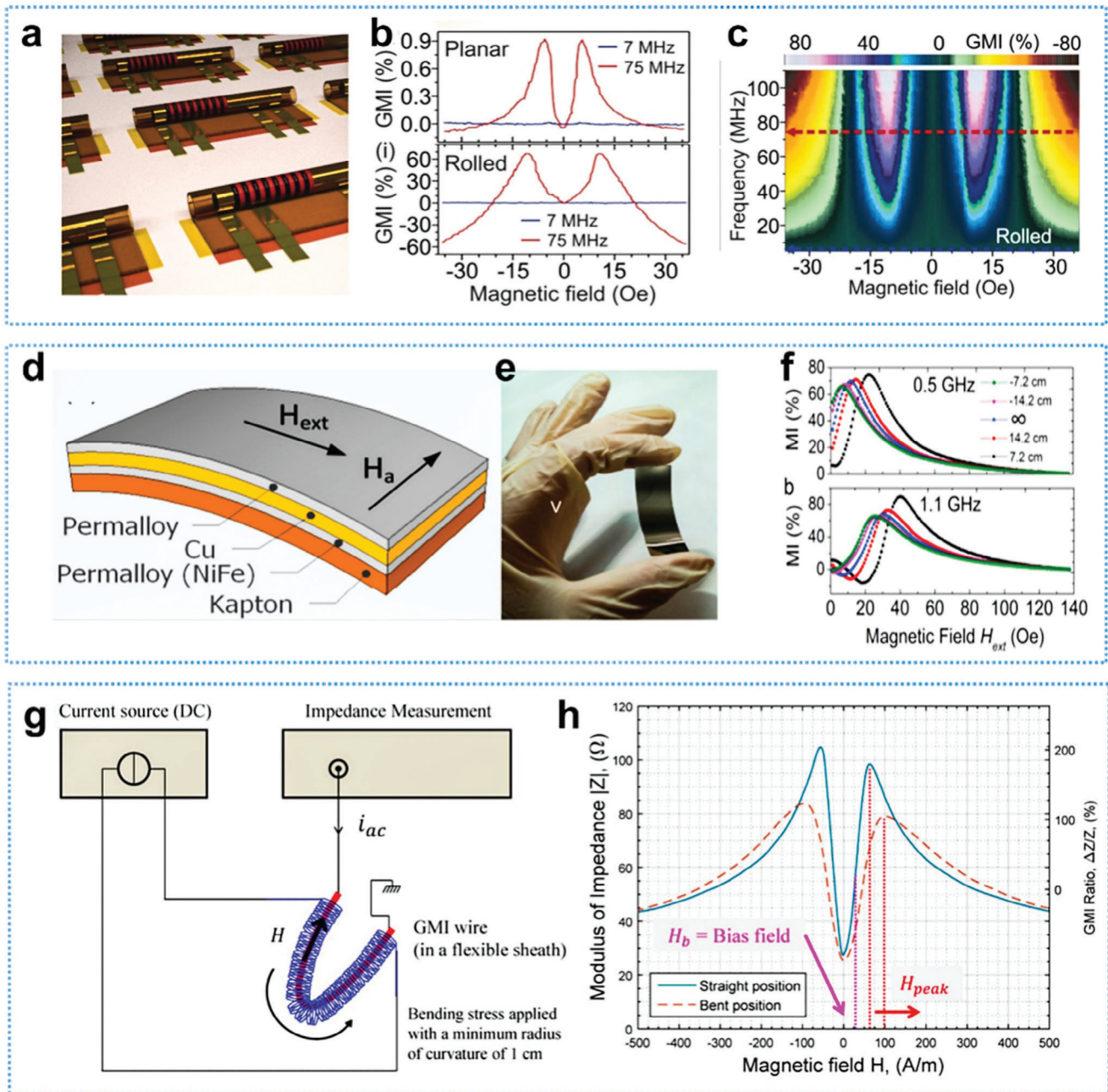


**Figure 21.** Flexible GMI sensor structure and its application. a) Array of self-assembled GMI sensors with pick-up coils.<sup>[166]</sup> b) Magnetic field dependence of the GMI response measured at 7 and 75 MHz using the planar and self-assembled structure.<sup>[166]</sup> c) 3D map of the GMI response versus frequency and magnetic field of the self-assembled device.<sup>[166]</sup> Copyright 2015, Wiley-VCH with a Creative Commons CC-BY license. d) Layer stack of a sensor on a Kapton substrate. Reproduced with permission.<sup>[167]</sup> Copyright 2015, IEEE. e) Optical image of the sensor. Reproduced with permission.<sup>[167]</sup> Copyright 2015, IEEE. f) MI ratio of the sample under different deflection levels at 0.5 and 1.1 GHz. Reproduced with permission.<sup>[167]</sup> Copyright 2015, IEEE. g) Principle diagram of GMI effect measurements under amorphous wire bending. Reproduced with permission.<sup>[168]</sup> h) Variations of  $|Z(H)|$  and  $\Delta Z/Z$  with bending stress. Reproduced with permission.<sup>[168]</sup> Copyright 2017, MDPI with a Creative Commons CC-BY license.

#### 4. Applications of Flexible Magnetosensitive Devices in Wearable Electronics

Flexible magnetosensitive sensors have attracted significant attention in the field of wearable electronics owing to their ability to conformally adhere to irregularly shaped surfaces, allow-

ing for seamless integration into wearable devices and touchless detection. These sensors hold immense promise in the field of wearable electronics, such as health monitoring and human-computer interactions. This section examines emerging applications of tactile sensing, biomagnetic detection, and geomagnetic navigation.

**Table 7.** Structure and performance of widely used GMI sensors.

Material	Substrate	GMI ratio	Sensitivity, frequency	Ref.
[FeNi/Ti]3/Cu/[Ti/FeNi]3	Cyclo-olefin copolymer	110%	23.7% per Oe, 180 MHz	[164]
NiFe/Cu/NiFe	Kapton	90%	9.2% per Oe, 1.1GHz	[165]
[FeNi/Ti]3/Cu/[FeNi/Ti]3	Copolymer	350%	45% per Oe, 60 MHz	[197]
NiFe/Cu/NiFe	Kapton	90%	9.2% per Oe, 1.1 GHz	[167]
NiFe/Cu/NiFe	PI	90%	50% per Oe, 75 MHz	[166]
NiFe/Cu/NiFe	Kapton	–	1.2 Ω Oe <sup>-1</sup> , 500 MHz	[198]
Co <sub>68.15</sub> Fe <sub>4.35</sub> Si <sub>12.25</sub> B <sub>15.25-x</sub> Cu <sub>x</sub> (x = 0, 1, 2, and 3 in atom%) amorphous wire	NA (wire diameter 45 ± 2 μm)	702%	–	[169]
(CoFeSiB/Ti)2 multilayer	PET	7.5%	–	[199]

#### 4.1. Tactile Sensing

Tactile sensing technology is crucial in human–robot interactions and object manipulation and has seen significant advancements with the development of flexible magnetosensitive devices. These devices are instrumental in various fields, showcasing exceptional performance in object manipulation and enhancing human–robot interactions.<sup>[174]</sup> The incorporation of flexible magnetic sensors in the development of tactile sensing devices involves a structural configuration that combines magnetic particles or films with magnetic sensors. The integration leverages the inherent qualities of increased sensitivity and capacity for non-contact operation, thereby facilitating the achievement of both enhanced sensitivity and multi-modal tactile detection.

Recently, Wu et al.<sup>[175]</sup> developed a bionic tactile perception sensor that utilized the GMI effect of CoFe-based wires. The sensor comprised a magnetic film and highly sensitive amorphous silk-based GMI sensor (Figure 24a–c). The impedance of the GMI sensor changed when pressure deformed the magnetic

film. Through the design of a back-end LC oscillation circuit, the sensor generated neural-like signals as output. The sensor could detect a force of 5 μN (or 0.3 Pa), which was significantly lower than the sensing threshold of human skin. Alfidhel et al.<sup>[176]</sup> developed a tactile sensing system by integrating highly elastic and permanent magnetic nanocomposite artificial cilia with GMI sensors. The nanocomposite was composed of iron nanowires (NWs) incorporated into PDMS. The cilia leveraged the permanent magnetic properties of the NWs, enabling remote operation with no additional magnetic field to magnetize the NWs. This not only reduced power consumption but also simplified system integration. Ge et al.<sup>[177]</sup> utilized a (Py/Cu) multilayer film structure as a magnetic sensing unit to create a bimodal electronic skin capable of contact and noncontact sensing. By combining a flexible magnetic film (Figure 24d,e), they demonstrated the usability of the bimodal electronic skin in AR settings. The dual sensing modes allowed for the complex selection and manipulation of virtual objects, laying a solid foundation for widespread applications in interactive electronics, human–computer interfaces, and medical science. Becker et al.<sup>[30]</sup> introduced a high-density integrated active-matrix magnetic sensor with the ability to sense 3D magnetic fields. This sensor delved into the complex vector nature of 3D magnetic fields and tracked magnetic objects in 3D space. Manufactured using micro-folding techniques, this sensor integrated AMR sensors into self-folding polymer stacks as sensing elements and embedded magnetic hairs. Real-time touch sensing was possible as the magnetic hairs detected contact, causing the magnetic particles within them to move, altering the 3D magnetic field of the entire device (Figure 24f,g).

Tactile signals obtained from flexible magnetoresistive sensors could be integrated with soft actuators to enable the activity of soft robots equipped with onboard sensing systems. This integration could facilitate the control of processes, such as assembly.<sup>[30,178,179]</sup> Ha et al.<sup>[179]</sup> employed magnetic field sensors as intelligent skin for magnetic soft robots. By leveraging the GMR effect to detect in-plane magnetic fields' strength and orientation, as well as anomalous Hall effect and GMR sensors to measure out-of-plane magnetic fields, the electronic skin demonstrated the ability to monitor its environment and adjust its behavior accordingly. This electronic skin could sense its orientation and displacement, detect its magnetization state, and prepare for folding (Figure 24h).

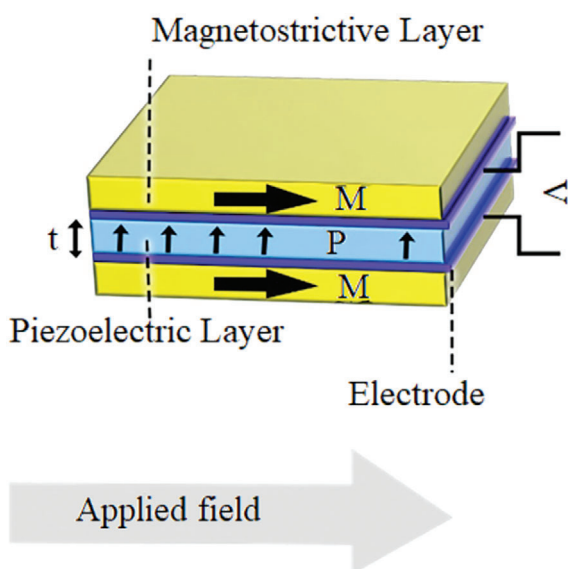


**Figure 22.** Schematic of an ME sensor.

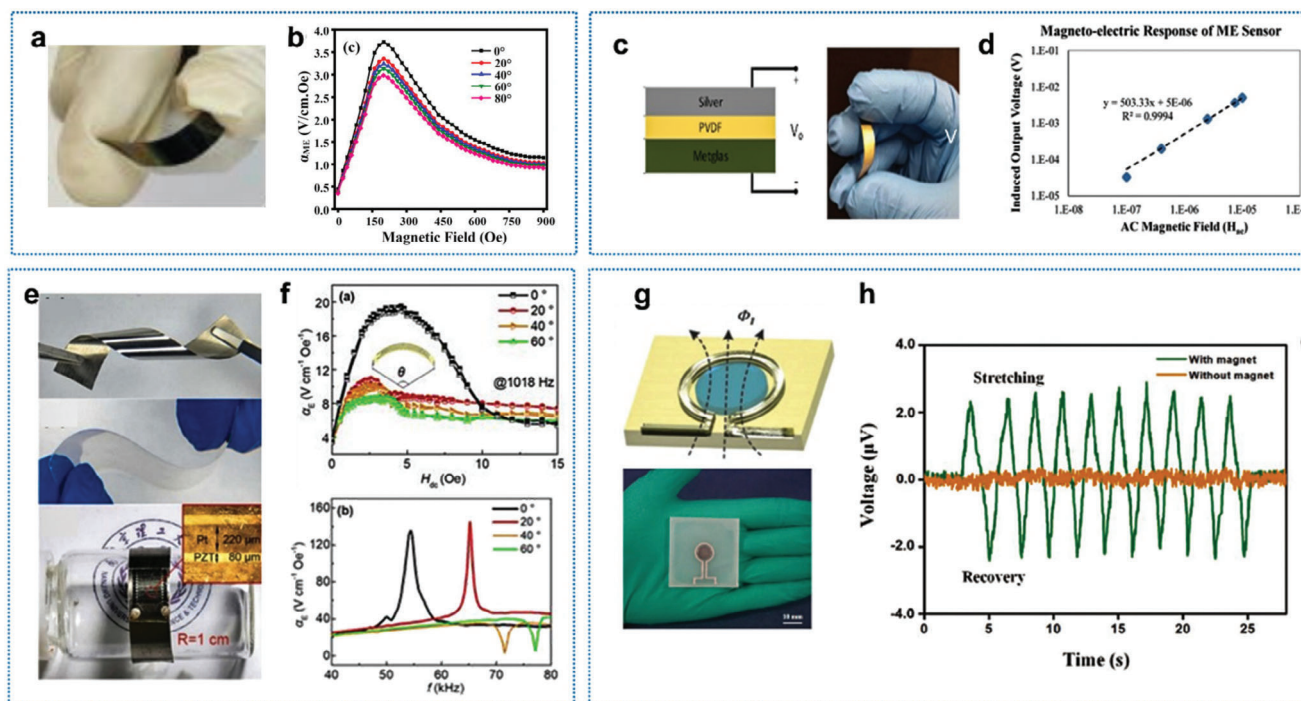


**Figure 23.** Flexible ME sensors and their properties. a) Actual image of a flexible ME sensor. Reproduced with permission.<sup>[192]</sup> Copyright 2023, AIP Publishing. b) Relationship between the flexible ME sensor and magnetic field under different bending conditions. Reproduced with permission.<sup>[192]</sup> Copyright 2023, AIP Publishing. c) Schematic of an ME sensor and the fabricated ME sensor. Reproduced with permission.<sup>[171]</sup> Copyright 2020, IOP Publishing. d) Flexible ME sensor output voltage as a function of AC magnetic field. Reproduced with permission.<sup>[171]</sup> Copyright 2020, IOP Publishing. e) Photograph of flexible Metglas foils and the layer-structured mica substrate. Reproduced with permission.<sup>[172]</sup> Copyright 2021, AIP Publishing with a Creative Commons CC-BY license. f) ME voltage coefficient  $\alpha E$  of the ME laminate in different bending conditions as a function of  $H_{dc}$  at a low frequency, and frequency at optimal  $H_{dc} = 4.5$  Oe. Reproduced with permission.<sup>[172]</sup> Copyright 2021, AIP Publishing with a Creative Commons CC-BY license. g) Schematic of the preparation of liquid metal-based stretchable ME devices and corresponding interaction mechanisms. Reproduced with permission.<sup>[173]</sup> Copyright 2020, Wiley-VCH. h) Sensor voltage output under strain. Reproduced with permission.<sup>[173]</sup> Copyright 2020, Wiley-VCH.

Multi-modal perception can acquire various types of signals simultaneously, thereby enhancing the functionality of tactile sensing. This approach is crucial for the advancement of magnetic-based tactile sensors. Ge et al.<sup>[177]</sup> developed a dual-function electronic skin equipped with a compatible magnetic micro-electromechanical system (MEMS) capable of converting tactile (through mechanical pressure) and noncontact (through magnetic fields) stimuli. By separating the electrical signals of tactile and non-contact interactions into distinct areas, the electronic skin can differentiate between these modes in real time. In addition, their inherent magnetic specificity overcomes the interference of irrelevant objects and facilitates signal-programmable interactions. This study allows a magnetic MEMS to enrich the complex interactions between virtual content data and physical objects in fields, such as AR, robotics, and healthcare.

#### 4.2. Geomagnetic Navigation

The advancement of flexible magnetosensitive skins, made possible by shapeable magnetoelectronics, presents the potential for artificial magnetoreception on seamless and comfortable on-skin platforms.<sup>[29]</sup> Moreover, integrated flexible magnetosensitive devices are expected to be instrumental in body-worn navigation systems, among other applications, providing motion tracking

and necessary feedback, which are crucial for wearable electronics and interactive devices.<sup>[27]</sup>

As shown in **Figure 25a,b**, Bermudez et al.<sup>[29]</sup> investigated a flexible AMR compass that conformed closely to human skin and not only detected the Earth's magnetic field but also maintained its functionality even when bent up to 150  $\mu\text{m}$ . This feature allows for accurate directional information in outdoor environments based on Earth's magnetic field with no external magnetic source. This compass can be utilized for the noncontact control of virtual units in gaming engines and as an interactive device for creating VR and AR applications. Xu et al.<sup>[82]</sup> fabricated a printable magnetoresistive sensor using an alternating magnetic field to actively drive the magnetic filler and guide the formation and self-healing of a percolation network (Figure 25c). These sensors boast low noise, high resolution, and ease of processing through various printing techniques, making them adaptable to different substrates. They hold promise for human-machine interfaces in safety applications, medical treatments, and AR.

In addition, conventional magnetic sensors can only perceive 1D or 2D field components and cannot fully explore the vector properties of the magnetic field. By depositing a (Py/CoFe)/Cu/(CoFe/Py)/IrMn spin-valve structure film onto a polyimide (PI) substrate to create 2D magnetic field sensors for detecting magnetic field components,

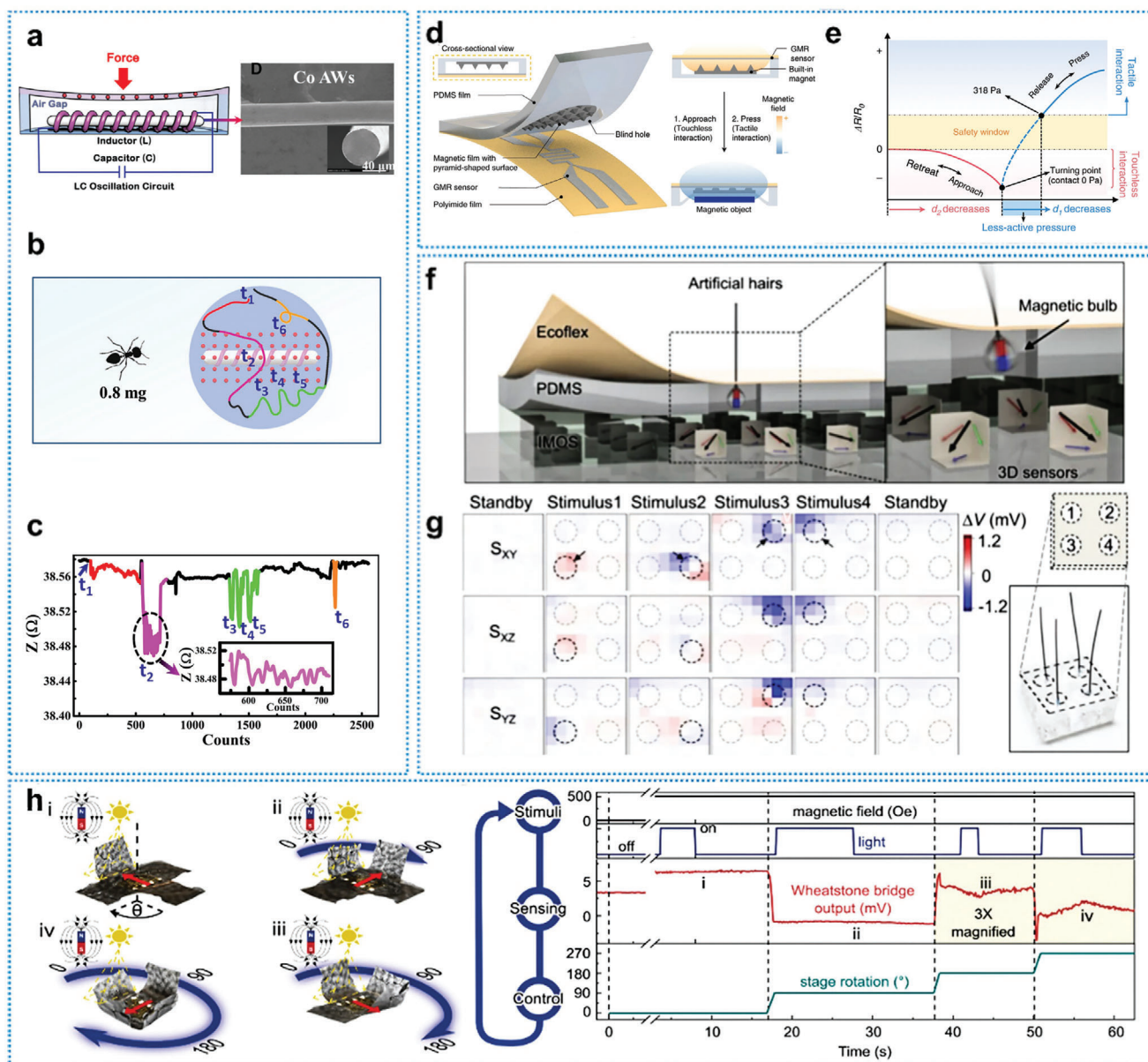


**Figure 24.** Application of flexible magnetic sensors in tactile perception. a) Highly sensitive bionic tactile sensor based on amorphous wire. Reproduced with permission.<sup>[187]</sup> Copyright 2018, AAAS. b,c) Demonstration of the sensor's response to ant movement. Reproduced with permission.<sup>[187]</sup> Copyright 2018, AAAS. d) Proximity pressure dual-mode sensor structure based on the GMR sensor. Reproduced with permission.<sup>[177]</sup> Copyright 2019, Springer Nature with a Creative Commons CC-BY license. e) Sensor response to proximity and pressure. Reproduced with permission.<sup>[177]</sup> Copyright 2019, Springer Nature with a Creative Commons CC-BY license. f) Vision of the devices for e-skin application. The stray field strength and direction of the hair-attached small magnets changed owing to bending of the hair, detectable by the sensor. Reproduced with permission.<sup>[30]</sup> Copyright 2022, Springer Nature with a Creative Commons CC-BY license. g) Sensor response to magnetic fields in different directions. Reproduced with permission.<sup>[30]</sup> Copyright 2022, Springer Nature with a Creative Commons CC-BY license. h) Sensors integrated with soft actuators for signal feedback. Reproduced with permission.<sup>[193]</sup> Copyright 2021, Wiley-VCH with a Creative Commons CC-BY license.

Bermudez et al.<sup>[180]</sup> achieved highly compliant magnetosensitive skins with directional awareness. These magneto-sensitive skins offered magnetic perception, body position tracking, and non-contact object manipulation (Figure 25d,e). This technology could be applied in the field of navigation, motion tracking in robotics, regenerative medicine, sports, gaming, and interactive applications in supplemented reality.

### 4.3. Biomagnetic Detection

Magnetic sensors, with their capability for noncontact measurement, allow for the noninvasive monitoring of various physiological parameters within the human body. These sensors can precisely locate magnetic markers within pharmaceuticals circulating in the bloodstream and internal body cavities,

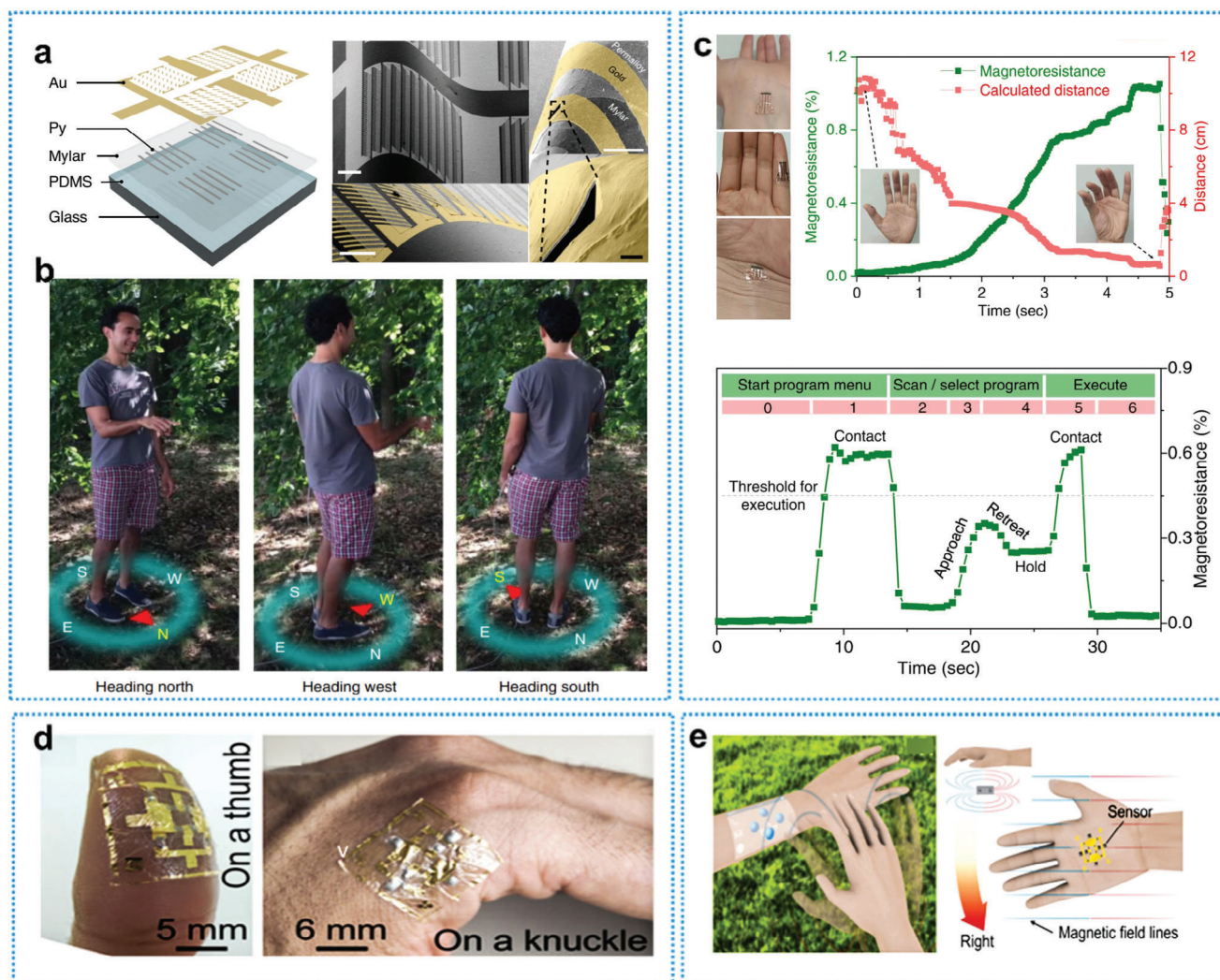


**Figure 25.** Application of flexible magnetic sensors in geomagnetic navigation and in human–computer interaction. a) AMR-based flexible magnetic sensor structure and physical illustration. Reproduced with permission.<sup>[29]</sup> Copyright 2018, Springer Nature. b) Detection of the direction of the earth’s magnetic field by the sensor to achieve geomagnetic navigation. Reproduced with permission.<sup>[29]</sup> Copyright 2018, Springer Nature. c) Flexible magnetic sensor utilized for detecting finger status. Reproduced with permission.<sup>[82]</sup> Copyright 2022, Springer Nature with a Creative Commons CC-BY license. d) Flexible AMR sensor attached to the hand, showcasing its high flexibility.<sup>[180]</sup> Copyright 2018, AAAS with a Creative Commons CC-BY license. e) Sensor detecting the direction of palm movement.<sup>[180]</sup> Copyright 2018, AAAS with a Creative Commons CC-BY license.

enabling the noninvasive detection of a wide range of biomagnetic signals.<sup>[153,181,182]</sup> This technology holds great promise in the medical domain.

Melzer et al.<sup>[183]</sup> introduced a novel concept for the in-flow detection of magnetic particles in millifluidics using elastic magnetic sensors that rely on the GMR effect. These sensors, owing to their stretchability, can be tightly wrapped around a fluidic channel. Subsequently, Lin et al.<sup>[184]</sup> developed a flexible microfluidic analytic device with an integrated high-performance GMR, allowing for precise probing of various dimensions of magnetic emulsion droplets with a limit of detection of 0.5 pL. This technology has broad applicability in high-throughput droplet screening, flow cytometry, and drug development (Figure 26a). Mönch et al.<sup>[185]</sup> developed a rolled-up magnetic sensor that relies on the GMR effect of magnetic [Py/Cu]<sub>30</sub> multi-

layers. They measured the response of the rolled-up GMR sensor to stray fields of magnetic particles passing through a microfluidic channel. This innovative approach has significant implications for the efficient biodetection of protein structures, disease diagnostics, and sorting of living cells (Figure 26b). Wu et al.<sup>[181]</sup> designed a rapid system for the sensitive noncontact detection of proteins using actuated magnetic particle tags. They utilized a magnetoelectric torque (MET) sensor to measure the tagged proteins. The system comprised a MET sensor with a magnet cantilever, and magnetic bead “test strips” were fabricated for testing. The performance of the MET sensor was evaluated using magnetic beads with a detection limit of 0.05 mg mL<sup>-1</sup>. In addition, the system successfully captured the alpha-fetoprotein biomarker using anti-AFP antibodies immobilized on the surface of the “test paper.” The biomarker

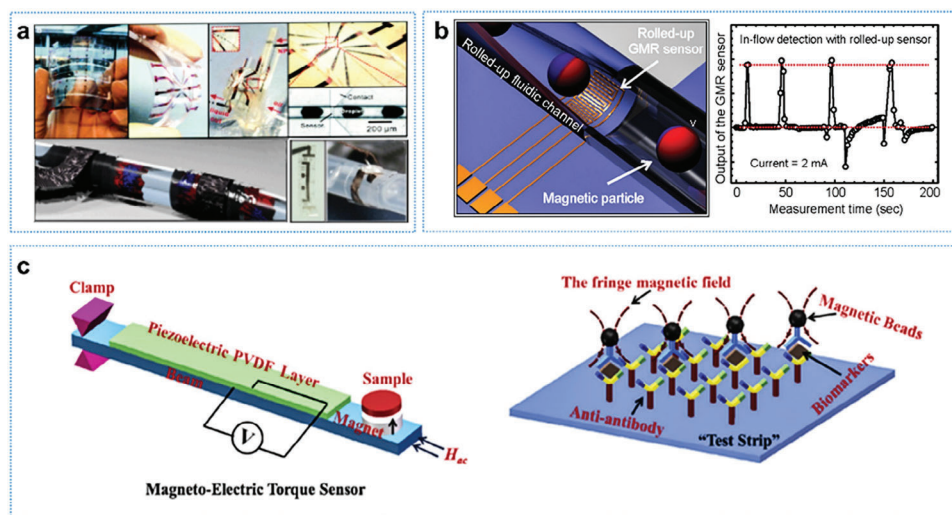


**Figure 26.** Application of flexible magnetic sensors in biomagnetic detection. a) GMR-based droplet analyzer for multiparametric analysis and sorting.<sup>[183,184]</sup> Reproduced with permission.<sup>[183,184]</sup> Copyright 2012, RSC Publishing. Copyright 2018, RSC Publishing with a Creative Commons CC-BY license. b) Rolled-up magnetic sensor for in-flow detection of magnetic objects. Reproduced with permission.<sup>[185]</sup> Copyright 2011, ACS Publications. c) Magneto-electric torque sensor utilized for detecting magnetic marker drugs. Reproduced with permission.<sup>[181]</sup> Copyright 2018, Elsevier B.V.

was then detected using anti-AFP antibody-labeled magnetic beads, with a detection limit of  $100 \text{ ng mL}^{-1}$  (Figure 26c).

## 5. Summary and Outlook

This study provided an overview of recent advancements in the field of flexible magnetosensitive materials and devices for wearable electronics. First, methods for fabricating flexible magnetosensitive materials, including metal and oxide magnetic materials, were introduced. In addition, the effect of stress/strain on the magnetic properties of flexible FM and AFM materials was explored, with a focus on aspects, such as MA and magnetic domain structures. Further, strategies for enhancing the stability of flexible magnetosensitive materials were outlined. Further, we provided a comprehensive overview of the types, structures, and functional principles of flexible magnetosensitive devices as well as their applications in the field of wearable electronics. Owing to their inherent advantages, such as flexibility, high sensitivity, and non-contact detection, flexible magnetosensitive devices exhibited promising potential in diverse areas, such as geomagnetic navigation, human–computer interaction, and human-like tactile sensing.

Despite the significant advancements, the large-scale production and application of flexible magnetosensitive materials and devices still encounter numerous challenges. Some key challenges include:

- Magnetic materials, typically composed of metals, alloys, and oxides, have a limited stretchability of  $\approx 2\%$ . Ensuring performance compatibility in parameters, such as sensitivity, linearity, and range, is challenging as well.
- Wearable devices are subjected to various environmental conditions, such as moisture, high temperatures, multidimensional deformation, and humidity. Ensuring the stability

and ruggedness of flexible magnetosensitive materials and devices remains a major challenge.

- Increasing the density of sensor arrays can result in increased crosstalk. However, flexible high-density magnetic sensor arrays present certain challenges.
- While flexible magnetic sensors are primarily utilized for detecting magnetic fields and pressure, achieving further multifunctional integration poses a challenge. Novel flexible magnetosensitive materials, sensing technologies, and system integration strategies should be explored in the future to develop multifunctional integrated flexible magnetic sensors. This will expand their applications in wearable electronics.

## Acknowledgements

H.Y. and S.L. contributed equally to this study. This research was partially supported by the National Natural Science Foundation of China (51931011, 52127803, 62174165, U20A6001, M-0152, U22A2075, and 51971233), the Chinese Academy of Sciences Youth Innovation Promotion Association (Y2022080), the “Pioneer” and “LeadingGoose” R&D Program of Zhejiang (2022C01032), the Natural Science Foundation of Zhejiang Province (LD22E010002, LD24E010001), the Ningbo Natural Science Foundation (20221JCGY010312), the Ningbo Key Research and Development Program (2023Z097), and the China Postdoctoral Foundation (2022M723251). [Correction added on June 17, 2024, after first online publication: Figures 1 + 18 has been updated.]

## Conflict of Interest

The authors declare no conflict of interest.

## Keywords

flexible magnetic devices, flexible magnetosensitive materials, mechanical regulations, wearable electronics

Received: November 11, 2023  
Revised: May 14, 2024  
Published online: May 29, 2024

- [1] Y. Liu, K. He, G. Chen, W. R. Leow, X. Chen, *Chem. Rev.* **2017**, *117*, 12893.
- [2] J. L. Wang, M. Hassan, J. W. Liu, S. H. Yu, *Adv. Mater.* **2018**, *30*, 1803430.
- [3] P. Wang, M. Hu, H. Wang, Z. Chen, Y. Feng, J. Wang, W. Ling, Y. Huang, *Adv. Sci.* **2020**, *7*, 2001116.
- [4] W. Gao, H. Ota, D. Kiriya, K. Takei, A. Javey, *Acc. Chem. Res.* **2019**, *52*, 523.
- [5] K. J. Baeg, J. Lee, *Adv. Mater. Technol.* **2020**, *5*, 2000071.
- [6] Y. Yang, W. Gao, *Chem. Soc. Rev.* **2019**, *48*, 1465.
- [7] S. Chen, J. Qi, S. Fan, Z. Qiao, J. C. Yeo, C. T. Lim, *Adv. Healthcare Mater.* **2021**, *10*, 2100116.
- [8] X. Wang, L. Dong, H. Zhang, R. Yu, C. Pan, Z. L. Wang, *Adv. Sci.* **2015**, *2*, 1500169.
- [9] B. Nie, S. Liu, Q. Qu, Y. Zhang, M. Zhao, J. Liu, *Acta Biomater.* **2022**, *139*, 280.
- [10] Q. Shi, B. Dong, T. He, Z. Sun, J. Zhu, Z. Zhang, C. Lee, *InfoMat* **2020**, *2*, 1131.
- [11] W. Shi, Y. Guo, Y. Liu, *Adv. Mater.* **2020**, *32*, 1901493.
- [12] Y. Chen, X. Fu, Y. Jiang, W. Feng, D. Yu, W. Wang, *Chem. Eng. J.* **2023**, *467*, 143408.
- [13] H. Zhang, D. Zhang, Z. Wang, G. Xi, R. Mao, Y. Ma, D. Wang, M. Tang, Z. Xu, H. Luan, *ACS Appl. Mater. Interfaces* **2023**, *15*, 5128.
- [14] R. Yin, D. Wang, S. Zhao, Z. Lou, G. Shen, *Adv. Funct. Mater.* **2020**, *31*, 2008936.
- [15] Y. Gao, V. V. Soman, J. P. Lombardi, P. P. Rajbhandari, T. P. Dhakal, D. G. Wilson, M. D. Poliks, K. Ghose, J. N. Turner, Z. Jin, *IEEE Trans. Instrum. Meas.* **2020**, *69*, 4314.
- [16] Y. Ma, Y. Zhang, S. Cai, Z. Han, X. Liu, F. Wang, Y. Cao, Z. Wang, H. Li, Y. Chen, X. Feng, *Adv. Mater.* **2020**, *32*, 1902062.
- [17] Y. Su, C. Ma, J. Chen, H. Wu, W. Luo, Y. Peng, Z. Luo, L. Li, Y. Tan, O. M. Omisore, Z. Zhu, L. Wang, H. Li, *Nanoscale Res. Lett.* **2020**, *15*, 200.
- [18] A. Nozariasmarz, H. Collins, K. Dsouza, M. H. Polash, M. Hosseini, M. Hyland, J. Liu, A. Malhotra, F. M. Ortiz, F. Mohaddes, V. P. Ramesh, Y. Sargolzaeiaval, N. Snouwaert, M. C. Öztürk, D. Vashae, *Appl. Energy* **2020**, *258*, 114069.
- [19] P. C. Y. Chow, T. Someya, *Adv. Mater.* **2020**, *32*, 1902045.
- [20] W. Heng, S. Solomon, W. Gao, *Adv. Mater.* **2022**, *34*, 2107902.
- [21] N. Wen, L. Zhang, D. Jiang, Z. Wu, B. Li, C. Sun, Z. Guo, *J. Mater. Chem. A* **2020**, *8*, 25499.
- [22] Y. Wu, Y. Li, Y. Zou, W. Rao, Y. Gai, J. Xue, L. Wu, X. Qu, Y. Liu, G. Xu, L. Xu, Z. Liu, Z. Li, *Nano Energy* **2022**, *92*, 106715.
- [23] W. Huang, L. Feng, G. Wang, E. Reichmanis, in *Flexible and Wearable Electronics for Smart Clothing*, Wiley, Hoboken, NJ **2020**, Ch.1, <https://doi.org/10.1002/9783527818556>.
- [24] J. Zhao, Y. Fu, Y. Xiao, Y. Dong, X. Wang, L. Lin, *Adv. Mater. Technol.* **2019**, *5*, 1900781.
- [25] T. Xing, A. He, Z. Huang, Y. Luo, Y. Zhang, M. Wang, Z. Shi, G. Ke, J. Bai, S. Zhao, F. Chen, W. Xu, *Chem. Eng. J.* **2023**, *474*, 145534.
- [26] J. Zhang, G. Chen, J. Chen, *Adv. Sens. Res.* **2022**, *1*, 2200008.
- [27] G. S. Cañón Bermúdez, D. Makarov, *Adv. Funct. Mater.* **2021**, *31*, 2007788.
- [28] A. Sasmal, A. Arockiarajan, *Nano Energy* **2023**, *115*, 108733.
- [29] G. S. Cañón Bermúdez, H. Fuchs, L. Bischoff, J. Fassbender, D. Makarov, *Nat. Electron.* **2018**, *1*, 589.
- [30] C. Becker, B. Bao, D. D. Karnaushenko, V. K. Bandari, B. Rivkin, Z. Li, M. Faghih, D. Karnaushenko, O. G. Schmidt, *Nat. Commun.* **2022**, *13*, 2121.
- [31] X. Zhang, J. Ai, R. Zou, B. Su, *ACS Appl. Mater. Interfaces* **2021**, *13*, 15727.
- [32] X. Han, H. Seki, Y. Kamiya, M. Hikizu, "Wearable handwriting input device using magnetic field", presented at SICE Annual Conference, Takamatsu, **2007**, <https://doi.org/10.1109/SICE.2007.4421009>.
- [33] S. Chen, Y. Chen, J. Yang, T. Han, S. Yao, *npj Flexible Electron.* **2023**, *7*, 1.
- [34] Y.-W. Liu, Q.-F. Zhan, R.-W. Li, *Chin. Phys. B* **2013**, *22*, 127502.
- [35] L. Jogschies, D. Klaas, R. Kruppe, J. Rittinger, P. Taptimthong, A. Wienecke, L. Rissing, M. C. Wurz, *Sensors* **2015**, *15*, 28665.
- [36] D. Makarov, M. Melzer, D. Karnaushenko, O. G. Schmidt, *Appl. Phys. Rev.* **2016**, *3*, 011101.
- [37] M. A. Khan, J. Sun, B. Li, A. Przybysz, J. Kosel, *Eng. Res. Express* **2021**, *3*, 022005.
- [38] D. Faurie, F. Zighem, A. Garcia-Sanchez, P. Lupo, A. O. Adeyeye, *Appl. Phys. Lett.* **2017**, *110*, 091904.
- [39] G. Dai, Q. Zhan, Y. Liu, H. Yang, X. Zhang, B. Chen, R.-W. Li, *Appl. Phys. Lett.* **2012**, *100*, 122407.
- [40] M. Li, H. Yang, Y. Xie, K. Huang, L. Pan, W. Tang, X. Bao, Y. Yang, J. Sun, X. Wang, S. Che, R.-W. Li, *Nano Lett.* **2023**, *23*, 8073.
- [41] M. Melzer, G. Lin, D. Makarov, O. G. Schmidt, *Adv. Mater.* **2012**, *24*, 6468.
- [42] S. Eimer, H. Cheng, J. Li, X. Zhang, C. Zhao, W. Zhao, *Sci. China Inf. Sci.* **2023**, *66*, 122408.
- [43] M. Melzer, D. Makarov, A. Calvimontes, D. Karnaushenko, S. Baunack, R. Kaltofen, Y. Mei, O. G. Schmidt, *Nano Lett.* **2011**, *11*, 2522.
- [44] S. Zhang, Q. Zhan, Y. Yu, L. Liu, H. Li, H. Yang, Y. Xie, B. Wang, S. Xie, R.-W. Li, *Appl. Phys. Lett.* **2016**, *108*, 102409.
- [45] H. Li, Q. Zhan, Y. Liu, L. Liu, H. Yang, Z. Zuo, T. Shang, B. Wang, R.-W. Li, *ACS Nano* **2016**, *10*, 4403.
- [46] L. Pan, Y. Xie, H. Yang, M. Li, X. Bao, J. Shang, R. W. Li, *Sensors* **2023**, *23*, 4083.
- [47] Y. Bitla, Y.-H. Chu, *FlatChem* **2017**, *3*, 26.
- [48] Y.-H. Chu, *npj Quantum Mater.* **2017**, *2*, 67.
- [49] W. Hou, Z. Zhou, L. Zhang, S. Zhao, B. Peng, Z. Hu, W. Ren, Z.-G. Ye, Z.-D. Jiang, M. Liu, *ACS Appl. Mater. Interfaces* **2019**, *11*, 21727.
- [50] H.-J. Liu, C.-K. Wang, D. Su, T. Amrillah, Y.-H. Hsieh, K.-H. Wu, Y.-C. Chen, J.-Y. Juang, L. M. Eng, S.-U. Jen, Y.-H. Chu, *ACS Appl. Mater. Interfaces* **2017**, *9*, 7297.
- [51] J. Liu, Y. Feng, R. Tang, R. Zhao, J. Gao, D. Shi, H. Yang, *Adv. Electron. Mater.* **2018**, *4*, 1700522.
- [52] M. Yen, Y.-H. Lai, C.-Y. Kuo, C.-T. Chen, C.-F. Chang, Y.-H. Chu, *Adv. Funct. Mater.* **2020**, *30*, 2004597.
- [53] C.-I. Li, J.-C. Lin, H.-J. Liu, M.-W. Chu, H.-W. Chen, C.-H. Ma, C.-Y. Tsai, H.-W. Huang, H.-J. Lin, H.-L. Liu, P.-W. Chiu, Y.-H. Chu, *Chem. Mater.* **2016**, *28*, 3914.
- [54] D. Zha, B. Wang, L. Yuan, Y. Xie, H. Yang, K. Huang, L. Yu, R.-W. Li, *J. Magn. Magn. Mater.* **2022**, *557*, 169465.
- [55] K. Huang, Y. Xie, H. Yang, M. Li, L. Pan, X. Bao, Z. He, W. Li, R. W. Li, *Adv. Mater. Interfaces* **2023**, *10*, 2202487.
- [56] H. S. Kum, H. Lee, S. Kim, S. Lindemann, W. Kong, K. Qiao, P. Chen, J. Irwin, J. H. Lee, S. Xie, S. Subramanian, J. Shim, S.-H. Bae, C. Choi, L. Ranno, S. Seo, S. Lee, J. Bauer, H. Li, K. Lee, J. A. Robinson, C. A. Ross, D. G. Schlom, M. S. Rzechowski, C.-B. Eom, J. Kim, *Nature* **2020**, *578*, 75.
- [57] D. Du, S. Manzo, C. Zhang, V. Saraswat, K. T. Genser, K. M. Rabe, P. M. Voyles, M. S. Arnold, J. K. Kawasaki, *Nat. Commun.* **2021**, *12*, 2494.
- [58] M. Hassan, S. Laureti, C. Rinaldi, F. Fagiani, S. Varotto, G. Barucca, N. Y. Schmidt, G. Varvaro, M. Albrecht, *Nanoscale Adv.* **2021**, *3*, 3076.

- [59] C. H. Lee, J. H. Kim, C. Zou, I. S. Cho, J. M. Weisse, W. Nemeth, Q. Wang, A. C. van Duin, T. S. Kim, X. Zheng, *Sci. Rep.* **2013**, *3*, 2917.
- [60] M. Donolato, C. Tollan, J. M. Porro, A. Berger, P. Vavassori, *Adv. Mater.* **2013**, *25*, 623.
- [61] M. Hassan, S. Laureti, C. Rinaldi, F. Fagiani, G. Barucca, A. Gerardino, N. Schmidt, M. Fix, M. Albrecht, G. Varvaro, *Appl. Surf. Sci.* **2023**, *635*, 157740.
- [62] Y. Zhang, L. Shen, M. Liu, X. Li, X. Lu, L. Lu, C. Ma, C. You, A. Chen, C. Huang, L. Chen, M. Alexe, C.-L. Jia, *ACS Nano* **2017**, *11*, 8002.
- [63] L. Shen, L. Wu, Q. Sheng, C. Ma, Y. Zhang, L. Lu, J. Ma, J. Ma, J. Bian, Y. Yang, A. Chen, X. Lu, M. Liu, H. Wang, C. L. Jia, *Adv. Mater.* **2017**, *29*, 1702411.
- [64] D. Lu, D. J. Baek, S. S. Hong, L. F. Kourkoutis, Y. Hikita, H. Y. Hwang, *Nat. Mater.* **2016**, *15*, 1255.
- [65] Z. Lu, Y. Yang, L. Wen, J. Feng, B. Lao, X. Zheng, S. Li, K. Zhao, B. Cao, Z. Ren, D. Song, H. Du, Y. Guo, Z. Zhong, X. Hao, Z. Wang, R.-W. Li, *npj Flexible Electron.* **2022**, *6*, 9.
- [66] Z. Lu, J. Liu, J. Feng, X. Zheng, L.-h. Yang, C. Ge, K.-j. Jin, Z. Wang, R.-W. Li, *APL Mater.* **2020**, *8*, 051105.
- [67] S. Shrestha, M. Coile, M. Zhu, M. Souri, J. Kim, R. Pandey, J. W. Brill, J. Hwang, J.-W. Kim, A. Seo, *ACS Appl. Nano Mater.* **2020**, *3*, 6310.
- [68] F. An, K. Qu, G. Zhong, Y. Dong, W. Ming, M. Zi, Z. Liu, Y. Wang, B. Qi, Z. Ding, J. Xu, Z. Luo, X. Gao, S. Xie, P. Gao, J. Li, *Adv. Funct. Mater.* **2020**, *30*, 2003495.
- [69] S. L. Guohua Dong, Mouteng Yao, Ziyao Zhou, Yong-Qiang Zhang, Xu Han, Zhenlin Luo, Junxiang Yao, Bin Peng, Zhongqiang Hu, Houbing Huang, Tingting Jia, Jianguy Li, Wei Ren, Zuo-Guang Ye, Xiangdong Ding, n Sun, Ce-Wen Nan, Long-Qing Chen, Ju Li, M. Liu, *Science* **2019**, *366*, 475.
- [70] L. M. Loong, W. Lee, X. Qiu, P. Yang, H. Kawai, M. Saeys, J.-H. Ahn, H. Yang, *Adv. Mater.* **2016**, *28*, 4983.
- [71] C. Barraud, C. Deranlot, P. Seneor, R. Mattana, B. Dlubak, S. Fusil, K. Bouzehouane, D. Deneuve, F. Petroff, A. Fert, *Appl. Phys. Lett.* **2010**, *96*, 072502.
- [72] Y. Xie, B. Wang, H. Yang, R.-W. Li, *AIP Adv.* **2020**, *10*, 025327.
- [73] D. Karnaushenko, T. Kang, V. K. Bandari, F. Zhu, O. G. Schmidt, *Adv. Mater.* **2020**, *32*, 1902994.
- [74] R. Streubel, J. Lee, D. Makarov, M. Y. Im, D. Karnaushenko, L. Han, R. Schafer, P. Fischer, S. K. Kim, O. G. Schmidt, *Adv. Mater.* **2014**, *26*, 316.
- [75] Q. Huang, Y. Zhu, *Adv. Mater. Technol.* **2019**, *4*, 1800546.
- [76] D. Karnaushenko, D. Makarov, C. Yan, R. Streubel, O. G. Schmidt, *Adv. Mater.* **2012**, *24*, 4518.
- [77] D. Makarov, D. Karnaushenko, O. G. Schmidt, *ChemPhysChem* **2013**, *14*, 1771.
- [78] D. Karnaushenko, D. Makarov, M. Stober, D. D. Karnaushenko, S. Baunack, O. G. Schmidt, *Adv. Mater.* **2015**, *27*, 880.
- [79] M. Ha, G. S. Canon Bermudez, T. Kosub, I. Monch, Y. Zabala, E. S. Oliveros Mata, R. Illing, Y. Wang, J. Fassbender, D. Makarov, *Adv. Mater.* **2021**, *33*, 2005521.
- [80] P. Gupta, D. D. Karnaushenko, C. Becker, I. E. Okur, M. Melzer, B. Özer, O. G. Schmidt, D. Karnaushenko, *Adv. Mater. Technol.* **2022**, *7*, 2200190.
- [81] E. S. Oliveros Mata, G. S. Cañón Bermúdez, M. Ha, T. Kosub, Y. Zabala, J. Fassbender, D. Makarov, *Appl. Phys. A* **2021**, *127*, 280.
- [82] R. Xu, G. S. Canon Bermudez, O. V. Pylypovskiy, O. M. Volkov, E. S. Oliveros Mata, Y. Zabala, R. Illing, P. Makushko, P. Milkin, L. Ionov, J. Fassbender, D. Makarov, *Nat. Commun.* **2022**, *13*, 6587.
- [83] E. S. Oliveros-Mata, C. Voigt, G. S. Cañón Bermúdez, Y. Zabala, N. M. Valdez-Garduño, M. Fritsch, S. Mosch, M. Kusnezoff, J. Fassbender, M. Vinnichenko, D. Makarov, *Adv. Mater. Technol.* **2022**, *7*, 2200227.
- [84] D. Cao, Z. Wang, L. Pan, H. Feng, X. Cheng, Z. Zhu, J. Wang, Q. Liu, G. Han, *Appl. Phys. A* **2016**, *122*, 938.
- [85] Z. Tang, B. Wang, H. Yang, X. Xu, Y. Liu, D. Sun, L. Xia, Q. Zhan, B. Chen, M. Tang, Y. Zhou, J. Wang, R.-W. Li, *Appl. Phys. Lett.* **2014**, *105*, 103504.
- [86] Y. W. Liu, B. M. Wang, Q. F. Zhan, Z. H. Tang, H. L. Yang, G. Liu, Z. H. Zuo, X. S. Zhang, Y. L. Xie, X. J. Zhu, B. Chen, J. L. Wang, R. W. Li, *Sci. Rep.* **2014**, *4*, 6615.
- [87] X. Wen, B. Wang, P. Sheng, S. Hu, H. Yang, K. Pei, Q. Zhan, W. Xia, H. Xu, R.-W. Li, *Appl. Phys. Lett.* **2017**, *111*, 142403.
- [88] R. Asai, S. Ota, T. Namazu, T. Takenobu, T. Koyama, D. Chiba, *J. Appl. Phys.* **2016**, *120*, 083906.
- [89] X. Chen, B. Wang, X. Wen, P. Sheng, D. Pravarthana, H. Yang, Y. Xie, H. Liu, X. Xu, R.-W. Li, *J. Magn. Magn. Mater.* **2020**, *505*, 166750.
- [90] S. Merabtine, F. Zighem, D. Faurie, A. Garcia-Sanchez, P. Lupo, A. O. Adeyeye, *Nano Lett.* **2018**, *18*, 3199.
- [91] G. Q. Gao, C. Jin, W. C. Zheng, X. Pang, D. X. Zheng, H. L. Bai, *Europhys. Lett.* **2018**, *123*, 17002.
- [92] T. D. Ha, J.-W. Chen, M. Yen, Y.-H. Lai, B.-Y. Wang, Y.-Y. Chin, W.-B. Wu, H.-J. Lin, J.-Y. Juang, Y.-H. Chu, *ACS Appl. Mater. Interfaces* **2020**, *12*, 46874.
- [93] S. Ota, Y. Hibino, D. Bang, H. Awano, T. Kozeki, H. Akamine, T. Fujii, T. Namazu, T. Takenobu, T. Koyama, D. Chiba, *Appl. Phys. Express* **2016**, *9*, 043004.
- [94] H. Matsumoto, S. Ota, T. Koyama, D. Chiba, *Appl. Phys. Lett.* **2021**, *118*, 022406.
- [95] J. Liu, J. Chen, Y. Zhang, S. Fu, G. Chai, C. Cao, X. Zhu, Y. Guo, W. Cheng, D. Jiang, Z. Zhao, Q. Zhan, *ACS Appl. Mater. Interfaces* **2021**, *13*, 29975.
- [96] Q. Zhu, R. Tang, F. Peng, S. Xu, G. Liang, R. Zhao, Y. Fang, L. You, X. Su, *Phys. Rev. Appl.* **2021**, *16*, 054006.
- [97] Y. Yu, Q. Zhan, J. Wei, J. Wang, G. Dai, Z. Zuo, X. Zhang, Y. Liu, H. Yang, Y. Zhang, S. Xie, B. Wang, R.-W. Li, *Appl. Phys. Lett.* **2015**, *106*, 162405.
- [98] W. Liu, M. Liu, R. Ma, R. Zhang, W. Zhang, D. Yu, Q. Wang, J. Wang, H. Wang, *Adv. Funct. Mater.* **2018**, *28*, 1705928.
- [99] W. Liu, R. Ma, M. Liu, H. Wang, *ACS Appl. Mater. Interfaces* **2018**, *10*, 32331.
- [100] W. H. Meiklejohn, C. P. Bean, *Phys. Rev.* **1957**, *105*, 904.
- [101] J. Nogués, I. K. Schuller, *J. Magn. Magn. Mater.* **1999**, *192*, 203.
- [102] B. G. Park, J. Wunderlich, X. Martí, V. Holý, Y. Kurosaki, M. Yamada, H. Yamamoto, A. Nishide, J. Hayakawa, H. Takahashi, A. B. Shick, T. Jungwirth, *Nat. Mater.* **2011**, *10*, 347.
- [103] X. S. Zhang, Q. F. Zhan, G. H. Dai, Y. W. Liu, Z. H. Zuo, H. L. Yang, B. Chen, R. W. Li, *Appl. Phys. Lett.* **2013**, *102*, 022412.
- [104] P. Sheng, Y. Xie, Y. Bai, B. Wang, L. Zhang, X. Wen, H. Yang, X. Chen, X. Li, R.-W. Li, *Appl. Phys. Lett.* **2019**, *115*, 242403.
- [105] Z. Zhang, E. Liu, W. Zhang, P. K. J. Wong, Z. Xu, F. Hu, X. Li, J. Tang, A. T. S. Wee, F. Xu, *ACS Appl. Mater. Interfaces* **2019**, *11*, 8258.
- [106] C. Feng, Y. Li, L. Wang, Y. Cao, M. Yao, F. Meng, F. Yang, B. Li, K. Wang, G. Yu, *Adv. Funct. Mater.* **2020**, *30*, 1909708.
- [107] N. S. Gusev, A. V. Sadovnikov, S. A. Nikitov, M. V. Sapozhnikov, O. G. Udalov, *Phys. Rev. Lett.* **2020**, *124*, 157202.
- [108] M. V. Sapozhnikov, R. V. Gorev, E. V. Skorokhodov, N. S. Gusev, A. V. Sadovnikov, O. G. Udalov, *Phys. Rev. B* **2022**, *105*, 024405.
- [109] Q. Yang, Y. Cheng, Y. Li, Z. Zhou, J. Liang, X. Zhao, Z. Hu, R. Peng, H. Yang, M. Liu, *Adv. Electron. Mater.* **2020**, *6*, 2000246.
- [110] B. Peng, Q. Y. Xie, W. L. Zhang, Z. Y. Zhong, *J. Appl. Phys.* **2007**, *101*, 09C511.
- [111] G. Dai, X. Xing, Y. Shen, X. Deng, *J. Phys. D: Appl. Phys.* **2019**, *53*, 055001.
- [112] W. Karboul-Trojet, D. Faurie, E. Ait-Yahiatène, Y. Roussigné, F. Mazaleyrat, S. M. Chérif, *J. Appl. Phys.* **2012**, *111*, 07A926.

- [113] J. Zhang, W.-K. Lee, R. Tu, D. Rhee, R. Zhao, X. Wang, X. Liu, X. Hu, X. Zhang, T. W. Odom, M. Yan, *Nano Lett.* **2021**, *21*, 5430.
- [114] G. Dai, Q. Zhan, H. Yang, Y. Liu, X. Zhang, Z. Zuo, B. Chen, R.-W. Li, *J. Appl. Phys.* **2013**, *114*, 173913.
- [115] X. Qiao, X. Wen, B. Wang, Y. Bai, Q. Zhan, X. Xu, R.-W. Li, *Appl. Phys. Lett.* **2017**, *111*, 132405.
- [116] M. Hassan, S. Laureti, C. Rinaldi, F. Fagiani, G. Barucca, F. Casoli, A. Mezzi, E. Bolli, S. Kaciulis, M. Fix, A. Ullrich, M. Albrecht, G. Varvaro, *ACS Appl. Mater. Interfaces* **2022**, *14*, 51496.
- [117] H. Matsumoto, S. Ota, T. Koyama, D. Chiba, *Appl. Phys. Express* **2022**, *15*, 033004.
- [118] P. Makushko, E. S. Oliveros Mata, G. S. Cañón Bermúdez, M. Hassan, S. Laureti, C. Rinaldi, F. Fagiani, G. Barucca, N. Schmidt, Y. Zabala, T. Kosub, R. Illing, O. Volkov, I. Vladymyrskyi, J. Fassbender, M. Albrecht, G. Varvaro, D. Makarov, *Adv. Funct. Mater.* **2021**, *31*, 2101089.
- [119] J. Zhao, Q. Guo, H. Yin, J. Zou, Z. Zhao, W. Cheng, D. Jiang, Q. Zhan, *Chin. Phys. B* **2020**, *29*, 117501.
- [120] J. Li, Q. Zhan, S. Zhang, J. Wei, J. Wang, M. Pan, Y. Xie, H. Yang, Z. Zhou, S. Xie, B. Wang, R.-W. Li, *Sci. Rep.* **2017**, *7*, 2837.
- [121] B. A. Kaidarova, W. Liu, L. Swanepoel, A. Almansouri, N. R. Gerald, C. M. Duarte, J. Kosel, *npj Flexible Electron.* **2021**, *5*, 2.
- [122] B. Uzlu, Z. Wang, S. Lukas, M. Otto, M. C. Lemme, D. Neumaier, *Sci. Rep.* **2019**, *9*, 18059.
- [123] H. Xu, Z. Zhang, R. Shi, H. Liu, Z. Wang, S. Wang, L. M. Peng, *Sci. Rep.* **2013**, *3*, 1207.
- [124] M. Melzer, J. I. Monch, D. Makarov, Y. Zabala, G. S. Canon Bermudez, D. Karnaushenko, S. Baunack, F. Bahr, C. Yan, M. Kaltenbrunner, O. G. Schmidt, *Adv. Mater.* **2015**, *27*, 1274.
- [125] J. I. Monch, F. Bahr, M. Melzer, D. Karnaushenko, D. Makarov, W. Hofmann, O. G. Schmidt, *IEEE Trans. Magn.* **2015**, *51*, 404004.
- [126] W. Thomson, *Proc. R. Soc. London* **1857**, *8*, 546.
- [127] N. Jiang, H. An, Y. Bai, B. Yang, S. Zhao, *J. Phys. Chem. C* **2023**, *127*, 9154.
- [128] A. Schuhl, F. N. Van Dau, J. R. Childress, *Appl. Phys. Lett.* **1995**, *66*, 2751.
- [129] L. Jogschies, J. Rittinger, D. Klaas, M. C. Wurz, *Procedia Technol.* **2016**, *26*, 162.
- [130] P. N. Granell, G. Wang, G. S. Cañón Bermudez, T. Kosub, F. Golmar, L. Steren, J. Fassbender, D. Makarov, *npj Flexible Electron.* **2019**, *3*, 3.
- [131] M. Kim, S. Oh, W. Jeong, A. Talantsev, T. Jeon, R. Chaturvedi, S. Lee, C. Kim, *IEEE Magn. Lett.* **2020**, *11*, 1.
- [132] Z. Wang, X. Wang, M. Li, Y. Gao, Z. Hu, T. Nan, X. Liang, H. Chen, J. Yang, S. Cash, N. X. Sun, *Adv. Mater.* **2016**, *28*, 9370.
- [133] B. Ozer, H. Piskin, N. Akdogan, *IEEE Sens. J.* **2019**, *19*, 5493.
- [134] P. Grunberg, R. Schreiber, Y. Pang, M. B. Brodsky, H. Sowers, *Phys. Rev. Lett.* **1986**, *57*, 2442.
- [135] M. N. Baibich, J. M. Broto, A. Fert, F. Nguyen Van Dau, F. Petroff, P. Etienne, G. Creuzet, A. Friederich, J. Chazelas, *Phys. Rev. Lett.* **1988**, *61*, 2472.
- [136] G. Binasch, P. Grunberg, F. Saurenbach, W. Zinn, *Phys. Rev. B* **1989**, *39*, 4828.
- [137] S. S. P. Parkin, K. P. Roche, T. Suzuki, *Jpn. J. Appl. Phys.* **1992**, *31*, L1246.
- [138] S. S. P. Parkin, *Appl. Phys. Lett.* **1996**, *69*, 3092.
- [139] Y.-f. Chen, Y. Mei, R. Kaltfofen, J. I. Mönch, J. Schumann, J. Freudenberger, H.-J. Klauß, O. G. Schmidt, *Adv. Mater.* **2008**, *20*, 3224.
- [140] M. Melzer, D. Karnaushenko, G. Lin, S. Baunack, D. Makarov, O. G. Schmidt, *Adv. Mater.* **2015**, *27*, 1333.
- [141] M. Melzer, M. Kaltenbrunner, D. Makarov, D. Karnaushenko, D. Karnaushenko, T. Sekitani, T. Someya, O. G. Schmidt, *Nat. Commun.* **2015**, *6*, 6080.
- [142] T. Uhrmann, L. Bär, T. Dimopoulos, N. Wiese, M. Rührig, A. Lechner, *J. Magn. Magn. Mater.* **2006**, *307*, 209.
- [143] L. Liu, Q. Zhan, H. Yang, H. Li, S. Zhang, Y. Liu, B. Wang, X. Tan, R.-W. Li, *AIP Adv.* **2016**, *6*, 035206.
- [144] M.-D. Cubells-Beltrán, C. Reig, J. Madrenas, A. De Marcellis, J. Santos, S. Cardoso, P. Freitas, *Sensors* **2016**, *16*, 939.
- [145] B. Bao, D. D. Karnaushenko, O. G. Schmidt, Y. Song, D. Karnaushenko, *Adv. Intell. Syst.* **2022**, *4*, 2100253.
- [146] N. Pérez, M. Melzer, D. Makarov, O. Ueberschär, R. Ecke, S. E. Schulz, O. G. Schmidt, *Appl. Phys. Lett.* **2015**, *106*, 153501.
- [147] N. Münzenrieder, D. Karnaushenko, L. Petti, G. Cantarella, C. Vogt, L. Bütthe, D. D. Karnaushenko, O. G. Schmidt, D. Makarov, G. Tröster, *Adv. Electron. Mater.* **2016**, *2*, 1600188.
- [148] M. Kondo, M. Melzer, D. Karnaushenko, T. Uemura, S. Yoshimoto, M. Akiyama, Y. Noda, T. Araki, O. G. Schmidt, T. Sekitani, *Sci. Adv.* **2020**, *6*, aay6094.
- [149] M. Julliere, *Phys. Lett. A* **1975**, *54*, 225.
- [150] A. Bedoya-Pinto, M. Donolato, M. Gobbi, L. E. Hueso, P. Vavassori, *Appl. Phys. Lett.* **2014**, *104*, 062412.
- [151] J. Gaspar, H. Fonseca, E. Paz, M. Martins, J. Valadeiro, S. Cardoso, R. Ferreira, P. P. Freitas, *IEEE Trans. Magn.* **2017**, *53*, 5300204.
- [152] S. Ota, A. Ando, T. Sekitani, T. Koyama, D. Chiba, *Appl. Phys. Lett.* **2019**, *115*, 202401.
- [153] S. Amara, G. A. T. Sevilla, M. Hawsawi, Y. Mashraei, H. Mohammed, M. E. Cruz, Y. P. Ivanov, S. Jaiswal, G. Jakob, M. Kläui, M. Hussain, J. Kosel, *Adv. Eng. Mater.* **2018**, *20*, 1800471.
- [154] A. Husmann, J. B. Betts, G. S. Boebinger, A. Migliori, T. F. Rosenbaum, M. L. Saboungi, *Nature* **2002**, *417*, 421.
- [155] M. N. Ali, J. Xiong, S. Flynn, J. Tao, Q. D. Gibson, L. M. Schoop, T. Liang, N. Haldolaarachchige, M. Hirschberger, N. P. Ong, R. J. Cava, *Nature* **2014**, *514*, 205.
- [156] N. Kumar, Y. Sun, N. Xu, K. Manna, M. Yao, V. Süß, I. Leermakers, O. Young, T. Förster, M. Schmidt, H. Borrmann, B. Yan, U. Zeitler, M. Shi, C. Felser, C. Shekhar, *Nat. Commun.* **2017**, *8*, 1642.
- [157] R. Niu, W. K. Zhu, *J. Phys.: Condens. Matter* **2021**, *34*, 113001.
- [158] L. V. Panina, K. Mohri, *Appl. Phys. Lett.* **1994**, *65*, 1189.
- [159] L. V. Panina, K. Mohri, T. Uchiyama, *Phys. A: Stat. Mech. Appl.* **1997**, *241*, 429.
- [160] S. Jiang, D. Xing, J. Liu, H. Shen, D. Chen, W. Fang, J. Sun, *J. Alloys Compd.* **2015**, *644*, 180.
- [161] L. P. Shen, T. Uchiyama, K. Mohri, E. Kita, K. Bushida, *IEEE Trans. Magn.* **1997**, *33*, 3355.
- [162] K. Mohri, T. Uchiyama, L. V. Panina, M. Yamamoto, K. Bushida, *J. Sens.* **2015**, *2015*, 718069.
- [163] C. Dolabdjian, D. Ménard, in *Smart Sensors, Measurement and Instrumentation*, Vol. 19 (Eds: A. Grosz, M. J. Haji-Sheikh, S. C. Mukhopadhyay), Springer, Basel, Switzerland **2017**, Ch.4, <https://doi.org/10.1007/978-3-319-34070-8>.
- [164] E. Fernandez, G. V. Kurlyandskaya, A. Garcia-Arribas, A. V. Svalov, *Nanoscale Res. Lett.* **2012**, *7*, 230.
- [165] K. Agra, T. J. A. Mori, L. S. Dorneles, V. M. Escobar, U. C. Silva, C. Chesman, F. Bohn, M. A. Corrêa, *J. Magn. Magn. Mater.* **2014**, *355*, 136.
- [166] D. Karnaushenko, D. D. Karnaushenko, D. Makarov, S. Baunack, R. Schafer, O. G. Schmidt, *Adv. Mater.* **2015**, *27*, 6582.
- [167] B. Li, M. N. Kavalzhiev, J. Kosel, *J. Magn. Magn. Mater.* **2015**, *378*, 499.
- [168] J. Nabias, A. Asfour, J. P. Yonnet, *Sensors* **2017**, *17*, 640.
- [169] S. Jiang, H. Wang, D. Estevez, Y. Huang, L. Zhang, H. Shen, Z. Ning, F. Qin, J. Sun, *Mater. Des.* **2021**, *204*, 109642.
- [170] A. Sasmal, S. Sen, P. S. Devi, *Phys. Chem. Chem. Phys.* **2019**, *21*, 5974.

- [171] A. A. Chlaihawi, S. Emamian, B. B. Narakathu, M. M. Ali, D. Maddipatla, B. J. Bazuin, M. Z. Atashbar, *Sens. Actuators, A* **2017**, 268, 1.
- [172] N. Yang, H. Wu, S. Wang, G. Yuan, J. Zhang, O. Sokolov, M. I. Bichurin, K. Wang, Y. Wang, *APL Mater.* **2021**, 9, 021123.
- [173] X. Zhang, J. Ai, Z. Ma, Y. Yin, R. Zou, B. Su, *Adv. Funct. Mater.* **2020**, 30, 2003680.
- [174] H. Hu, C. Zhang, C. Pan, H. Dai, H. Sun, Y. Pan, X. Lai, C. Lyu, D. Tang, J. Fu, P. Zhao, *ACS Nano* **2022**, 16, 19271.
- [175] Y. Wu, Y. Liu, Y. Zhou, Q. Man, C. Hu, W. Asghar, F. Li, Z. Yu, J. Shang, G. Liu, M. Liao, R.-W. Li, *Sci. Rob.* **2018**, 3, aat0429.
- [176] A. Alfidhel, B. Li, A. Zaher, O. Yassine, J. Kosel, *Lab Chip* **2014**, 14, 4362.
- [177] J. Ge, X. Wang, M. Drack, O. Volkov, M. Liang, G. S. Canon Bermudez, R. Illing, C. Wang, S. Zhou, J. Fassbender, M. Kaltenbrunner, D. Makarov, *Nat. Commun.* **2019**, 10, 4405.
- [178] B. Rivkin, C. Becker, F. Akbar, R. Ravishankar, D. D. Karnaushenko, R. Naumann, A. Mirhajivarzaneh, M. Medina-Sánchez, D. Karnaushenko, O. G. Schmidt, *Adv. Intell. Syst.* **2021**, 3, 2000238.
- [179] M. Ha, G. S. Cañón Bermúdez, J. A. C. Liu, E. S. Oliveros Mata, B. A. Evans, J. B. Tracy, D. Makarov, *Adv. Mater.* **2021**, 33, 2008751.
- [180] G. S. Canon Bermudez, D. D. Karnaushenko, D. Karnaushenko, A. Lebanov, L. Bischoff, M. Kaltenbrunner, J. Fassbender, O. G. Schmidt, D. Makarov, *Sci. Adv.* **2018**, 4, aao2623.
- [181] Y. Wu, Y. Liu, F. Li, Y. Zhou, J. Ding, R.-W. Li, *Sens. Actuators, B* **2018**, 276, 540.
- [182] G. Y. Melnikov, V. N. Lepalovskij, A. V. Svalov, A. P. Safronov, G. V. Kurlyandskaya, *Sensors* **2021**, 21, 3621.
- [183] M. Melzer, D. Karnaushenko, D. Makarov, L. Baraban, A. Calvimontes, I. Mönch, R. Kaltofen, Y. Mei, O. G. Schmidt, *RSC Adv.* **2012**, 2, 2284.
- [184] G. Lin, D. Makarov, M. Melzer, W. Si, C. Yan, O. G. Schmidt, *Lab Chip* **2014**, 14, 4050.
- [185] I. Monch, D. Makarov, R. Koseva, L. Baraban, D. Karnaushenko, C. Kaiser, K. F. Arndt, O. G. Schmidt, *ACS Nano* **2011**, 5, 7436.
- [186] Y. Zhao, S. Gao, X. Zhang, W. Huo, H. Xu, C. Chen, J. Li, K. Xu, X. Huang, *Adv. Funct. Mater.* **2020**, 30, 2001553.
- [187] Y. Wu, J. K. Yim, J. Liang, Z. Shao, M. Qi, J. Zhong, Z. Luo, X. Yan, M. Zhang, X. Wang, R. S. Fearing, R. J. Full, L. Lin, *Sci. Rob.* **2019**, 4, eaax1594.
- [188] Y. Yan, Z. Hu, Z. Yang, W. Yuan, C. Song, J. Pan, Y. Shen, *Sci. Rob.* **2021**, 6, eabc8801.
- [189] H.-L. Yang, Y.-L. Xie, Z.-X. Lu, Z.-M. Wang, R.-W. Li, *Acta Phys. Sin.* **2022**, 71, 097503.
- [190] G. Dai, X. Xing, Y. Shen, X. Deng, *J. Phys. D: Appl. Phys.* **2020**, 53, 055001.
- [191] J. Y. Chen, Y. C. Lau, J. M. Coey, M. Li, J. P. Wang, *Sci. Rep.* **2017**, 7, 42001.
- [192] D. Arora, P. Kumar, S. Singh, A. Goswami, D. Kaur, *Appl. Phys. Lett.* **2023**, 122, 263501.
- [193] M. Ha, G. S. Canon Bermudez, J. A. Liu, E. S. Oliveros Mata, B. A. Evans, J. B. Tracy, D. Makarov, *Adv. Mater.* **2021**, 33, 2008751.
- [194] S. S. Hong, M. Gu, M. Verma, V. Harbola, B. Y. Wang, D. Lu, A. Vailionis, Y. Hikita, R. Pentcheva, J. M. Rondinelli, H. Y. Hwang, *Science* **2020**, 368, 71.
- [195] C. Jin, Y. Zhu, X. Li, F. An, W. Han, Q. Liu, S. Hu, Y. Ji, Z. Xu, S. Hu, M. Ye, G. Zhong, M. Gu, L. Chen, *Adv. Sci.* **2021**, 8, 2102178.
- [196] Z. Wang, M. Shaygan, M. Otto, D. Schall, D. Neumaier, *Nanoscale* **2016**, 8, 7683.
- [197] G. V. Kurlyandskaya, E. Fernández, A. Svalov, A. Burgoa Beitia, A. García-Arribas, A. Larrañaga, *J. Magn. Magn. Mater.* **2016**, 415, 91.
- [198] A. Alfidhel, J. Kosel, *Adv. Mater.* **2015**, 27, 7888.
- [199] F. Jin, L. Xu, J. F. Jiang, B. Yang, Z. Zhao, K. F. Dong, J. L. Song, W. Q. Mo, Y. J. Hui, *J. Magn. Magn. Mater.* **2021**, 540, 168463.



**Yuanzhao Wu** received her Ph.D. from the University of Chinese Academy of Sciences in 2019 and is currently an associate researcher at the Ningbo Institute of Materials Technology and Engineering, Chinese Academy of Sciences. Her primary research focuses are flexible magnetic sensor devices and bionic devices.



**Yiwei Liu** received his B.S. and M.S. degrees from the Tianjin University in 2005 and 2007. In July 2008, he joined the Ningbo Institute of Materials Technology and Engineering (NIMTE), Chinese Academy of Sciences (CAS) as an assistant researcher. He received the Ph.D. degree from the NIMTE in 2015, and then, became an associate professor and professor in 2014 and 2019. His research interests include flexible/elastic sensitive materials and sensors, as well as their applications in human–computer interaction, motion monitoring, and health monitoring.



**Run-Wei Li** received his Ph.D. degree from the Institute of Physics (IOP), CAS in 2002. In 2008, he joined the Ningbo Institute of Materials Technology and Engineering (NIMTE), CAS, as a professor. Currently, he serves as senior member of the Institute of Electrical and Electronics Engineers (IEEE), the Fellow of the Chinese Institute of Electronics (CIE), and the Vice Chairman of the Applied Magnetics Committee of the CIE and the Magnetics Committee of the Chinese Physical Society (CPS). His research focuses on flexible magnetic and electronic materials and devices for information sensor and storage technologies.